UNIVERSITY OF OKLAHOMA

GRADUATE COLLEGE

INVESTIGATION INTO MOLECULAR BEAM EPITAXIAL GROWTH AND CHARACTERIZATION OF INGAAS STRUCTURES AND INAS SUPERLATTICES

A DISSERTATION

SUBMITTED TO THE GRADUATE FACULTY

in partial fulfillment of the requirements for the

Degree of

DOCTOR OF PHILOSOPHY

By

SANGEETHA VIJEYARAGUNATHAN
Norman, Oklahoma
2014

INVESTIGATION INTO MOLECULAR BEAM EPITAXIAL GROWTH AND CHARACTERIZATION OF INGAAS STRUCTURES AND INAS SUPERLATTICES

A DISSERTATION APPROVED FOR THE
HOMER L. DODGE DEPARTMENT OF PHYSICS AND ASTRONOMY

BY

_____
Dr. Michael B. Santos, Chair

_____
Dr. Kieran Mullen

_____
Dr. Sheena Q. Murphy

_____
Dr. John Moore-Furneaux

_____
Dr. Patrick J. McCann

Acknowledgements

I would like to express my sincere gratitude to my advisor, Professor Michael Santos, for his invaluable contributions of time, ideas, funding and guidance throughout my PhD program. I am grateful to him for providing me the platform to learn and shape my research goals in the right direction. I am indebted for the training I have received through this work that will continue to be of value moving forward.

I would also like to thank Dr. Ian Sellers for the device design on superlattice structures and his collaborators at Institute of Solid State Electronics, Vienna University of Technology, Austria for their assistance with XRD measurements. I am also thankful to my reading committee members Dr. Kieran Mullen, Dr. Sheena Q. Murphy, Dr. John Moore-Furneaux, and Dr. Patrick J. McCann for their inputs. My thanks are due to Tetsuya Mishima for his help and guidance in the maintenance of the parts and equipments in MBE and also for readily sharing his years of knowledge whenever I had a question. I am thankful to Joel Keay for the training on characterization techniques. I sincerely thank the students and postdocs of III-V MBE group and the photovoltaics group at OU, for their assistance in various experiments.

I am most grateful to my family and my friends who have become family for all their support and love.

The research in this dissertation was supported by funding from Intel Corporation, the Japan Science and Technology Agency, and the National Science Foundation.

Table of Contents

List of Tables

List of Figures

Abstract

InGaAs quantum wells have been experimentally studied for their potential application in electronic devices. The narrow band gap of InGaAs lead to smaller effective masses for electrons and holes, which results in higher mobilities in the well. In this work, the layer structure, doping and growth parameters of InGaAs wells were further optimized to obtain a higher density and mobility. At room temperature, an electron density of $2.2\times10^{12}cm^{-2}$ with mobility of $12{,}800cm^2/Vs$ has been achieved in $In_{0.64}Ga_{0.36}As$ quantum well.

Source and drain regions of InGaAs based field-effect-transistors need to be heavily doped for low contact resistance. We studied doping efficiency at higher concentrations in $In_{0.53}Ga_{0.47}As$ using Si as the n-type and Be as the p-type dopant. The maximum doping concentration achieved for n and p doping are $4.8\times10^{19}cm^{-3}$ and $1.3\times10^{20}cm^{-3}$, respectively.

The carrier multiplication effect is an emerging research area in the next generation solar cell techniques. Favorable energy levels for carrier multiplication can be achieved in InAs/AlAsSb superlattices through quantum confinement. In this work, a series of InAs/AlAsSb superlattice structures were grown by molecular beam epitaxy on GaAs (001) and InAs (001) substrates. Structural assessment from high-resolution x-ray diffraction shows good compositional control of the superlattices. The superlattice structures display peak photoluminescence energies in the designed 0.7-0.8 eV spectral region.

Chapter 1: Molecular Beam Epitaxy and Basics of Quantum Structures

1.1 Introduction

This dissertation investigates the growth of group III-V semiconductor structures for electronic applications, solar cell applications and basic condensed matter research using the Molecular Beam Epitaxy (MBE) growth technique.

Molecular Beam Epitaxy is a leading semiconductor growth technique used in producing a range of electronic and optoelectronic devices which include high speed transistors, solid-state lasers, and high-efficiency solar cells. Its capacity to grow high-quality complex structures makes MBE well suited for our area of investigation and material choices.

High speed electronics, built on semiconductor structures, is a continuously evolving market where devices are now reaching a performance limit with existing manufacturing materials and techniques. Group III-V semiconductors are considered as a potential successor to the existing Silicon technology for electronic applications. The mobility of carriers is a fundamental figure of merit of a material to build high performance devices with. Compared to Si, III-V semiconductors have higher intrinsic carrier mobilities. These mobilities can be manipulated through design and optimization of quantum structures through which scattering mechanisms of carriers can be suppressed to further increase the mobility. The investigation area in this dissertation for electronic applications is subdivided into doping efficiency- increasing carriers of a

pure semiconductor- and quantum structures studies. The doping studies involve understanding doping limitations and optimizing growth conditions for increased dopant incorporation. The quantum structure investigation involves optimizing design parameters and growth conditions to obtain intended and consistent transport properties; i.e., high density and high mobility of carriers. The ultimate goals of this study are producing structures with superior transport properties than Si and finding material and technical solutions for problems as they arise for III-V integration with Silicon technology, from the MBE growth point of view.

Solar cells are an active area of research and implementation as solar power is considered to be a clean and renewable energy source. Conventional Si cells, that absorb energy only over a certain wavelength range, suffer from low efficiencies. They are also reaching their theoretical efficiency limit. Alternative ideas to the conventional technology have been pursued in an effort to utilize the full solar spectrum and increase efficiencies. The III-V materials have suitable properties to explore a potential solar cell design, fundamentally different from the conventional cells, which can yield higher efficiencies. Such a structure is designed, modeled, grown and characterized. This project is particularly challenging as less knowledge exists about the material combination and a layer of the proposed III-V solar cell is known as a difficult alloy to grow. Initial steps of this investigation involve organization of the project flow and test structures, optimizing growth conditions, characterizations and understanding data for the project to evolve towards building a functioning solar device.

Chapter 1 of this dissertation describes the basics of MBE and quantum structures. Chapter 2 discusses the techniques used to characterize the MBE grown structures, from which the important properties of the structures are determined. The doping efficiency study is presented in chapter 3. The high mobility and high density structures are discussed in chapter 4. Chapter 5 describes the investigation of structures for solar cell application.

The first part of chapter 1 describes the Intevac Gen-II MBE system installed at the University of Oklahoma, Department of Physics and Astronomy for the growth of III-V semiconductor heterostructures. The following sections of part I cover the essential aspects of MBE technique. The MBE group recently acquired a new MBE system, a Veeco GENxplor, and its operation is underway.

In the second part of this chapter, useful concepts on quantum structures relevant to this dissertation are discussed.

Part I

1.2 MBE Layout and Basic Components

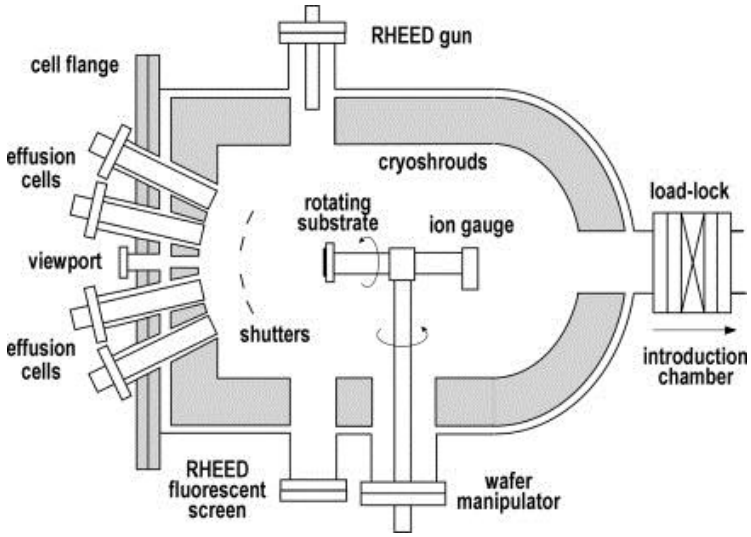

Figure 1.1 Schematic of a Gen II MBE growth chamber. (Secondo Franchi, *"Chapter 1 - Molecular beam epitaxy: fundamentals, historical background and future prospects", Molecular Beam Epitaxy*, Oxford, 2013).

MBE layout:

The Gen II Intevac MBE system at the University of Oklahoma has a modular design. These modules made of stainless steel are optimized for loading and unloading of wafers (load/lock chamber), growth preparation and storage (buffer chamber), and the growth process (growth chamber). Each of these chambers is individually pumped and separated by gate valves. Except for the load/lock chamber, other modules are always under ultra-high vacuum (UHV). The base pressure in the growth chamber is in the order of ~10^{-11} Torr, while the other chambers are at ~10^{-10} Torr. The load lock chamber is exposed to atmosphere each time wafers are loaded or extracted from the system,

without impairing UHV conditions of the others, and baked for a few hours before making any wafer transfer to the connecting chamber.

The main part of the process occurs in the growth chamber. The basic elements of a growth chamber are (i) the volume enclosed by liquid N_2 cooled cryoshrouds (ii) cells to produce atomic or molecular beams (iii) shutters that switches the beam on and off (iv) a heatable rotating substrate holder (v) an ion-gauge for beam flux measurements (v) an electron gun and fluorescent screen unit to monitor the wafer surface and (vi) a mass spectrometer for residual gas analysis and leak check. The schematic of Gen II growth module is shown in fig 1.1[1].

1.3 Beam Sources and Effusion Cells

There are 8 effusion cell ports in the Gen II system. Seven of them are used as source ports and one is used as a viewing port. The beam sources consist of three group III mono-atomic elements (In, Ga and Al), two group V tetra-atomic elements (As_4 and Sb_4), and two dopant elements for p-type and n-type doping (Be and Si). Effusion cells of mono-atomic sources essentially have a single-zone heating design for generating monomers. Tetra-atomic sources are heated in two stages, where one zone is at a higher temperature than the other to disassociate tetramer into dimers. In addition to two-zone heating, the Arsenic effusion cell also has a needle valve to control the As_2 beam flux entering the growth chamber. The sources of molecular beams are among the most essential components of the MBE system. They must operate at high temperatures (500°C-1300°C) and produce high purity, uniform beams across the wafer surface. For

this purpose, ultra-pure grade source materials are placed in a high-purity pyrolitic boron nitride conically shaped crucibles and heated radiatively by Ta wires, except for As and Sb. The Ta ribbons are heated by the Joule effect. Cell temperature is measured by thermocouples in contact with the cell-bottom or sidewalls. Cells are thermally isolated by heat shields filled with alcohol at a temperature -32°C. The flux density of a beam incident on the substrate surface is controlled by the temperature of the effusion cell which is regulated through proportional (P), integral (I), derivative (D) controllers. Shutters in front of the cells have a very short movement times in the order of 0.1s. As a result of the UHV conditions of the environment, MBE growth takes place in a molecular regime (i.e. mean free paths of atoms or molecules are larger than the critical lengths of the growth system). The short actuation times of the shutters and growth in the molecular regime enable abrupt changes in composition of the mixing phase. As a result, layers of thickness less than one tenth of a monolayer (ML) and abrupt doping profiles can be obtained. Such abrupt interfaces at atomic scales are crucial to observe quantum confinement. To avoid a concentration gradient across the surface, which occurs due to converging beam angles, the substrate is manipulated through a CAR (continuous azimuthal rotation) assembly.

1.4 Creating UHV Conditions

The UHV conditions of the MBE growth chamber minimize incorporation of unintentional impurities and optimize surface morphology. After opening the system to the atmosphere, UHV conditions are achieved in two steps. The chamber is initially pumped down to a pressure of ~1-100mTorr using a diaphragm pump and molecular

drag pump mounted on a cart. Then a combination of closed-cycle helium and ion pumps bring the pressure down to UHV levels. The chamber is also equipped with a Titanium sublimation pump for additional pumping capacity. Cryopanels cooled with liquid nitrogen, located around the chamber wall, remove condensable contaminants. Entry-exit and buffer chambers are connected to a closed-cycle helium pump, and ion pump respectively to obtain and maintain UHV conditions.

1.5 Growth Monitoring and Optimization Using RHEED Patterns

Reflection High-Energy Electron Diffraction (RHEED) is a real time surface analytical technique in MBE to inspect surface roughness and reconstruction. An electron gun produces a collimated beam of high energy electron (~10keV) which is diffracted off a growing surface and forms patterns in a fluorescent screen (figure 1.2)[2]. These patterns are captured by a CCD camera and analyzed with KSA 4000 software. RHEED diagnostics are extensively used for three purposes- to verify growth quality, observe surface reconstruction patterns, and to determine growth rates of source beams.

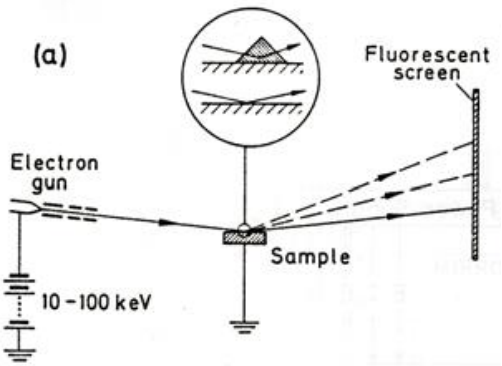

Figure 1.2: Schematic diagram of RHEED set-up. (M. A. Herman and H. Sitter, *Molecular Beam Epitaxy- Fundamentals and Current Status*, Springer, 1996).

The electron beam is directed at the surface at an angle in the order of 0.5- 3 degrees. At this low angle, electrons can see the diffracting planes only up to a few monolayers. If these monolayers are atomically smooth, then the electron beam is diffracted by a 2D lattice whose reciprocal lattice is parallel lines. When electrons see an atomically rough surface, they sense a 3D lattice and electrons can emerge from deeper planes. In this case, the reciprocal lattice is represented by points. Therefore if the diffraction pattern consists of streaks, rather than spots, it is good evidence that the pattern emerged from the top few planes and the surface is atomically smooth.

Surface atoms, left with unsaturated bonds, rearrange themselves to minimize surface energy. These new positions are different from bulk positions and the features due to the reconstruction appear between the sharp diffraction peaks of the bulk. Surface reconstruction patterns are useful in calibrating the growth temperature. For example, InSb undergoes a phase transition from asymmetric (1×3) to $c(4 \times 4)$ with a V/III ratio of 1.2 at substrate temperature ~ 340°C. They can also verify the correct stoichiometric growth. For example, the In rich regime shows a (4×2) and the reconstruction changes to $c(4 \times 4)$ if the surface becomes Sb rich[3]. The group V limited and substrate temperature dependent phase transition for InAs is (2×4) to (4×2) [4]. AlSb undergoes a $c(4 \times 4)$ to (1×3) transition[4]. The transition pattern of GaSb is (2×5) to (1×3) [4].

1.6 Growth Rate Calibration Using RHEED Intensity Oscillations

Growth rates and corresponding fluxes of source beams are calibrated as a function of cell temperature. It is useful to have both records to assess the accuracy of growth parameters as source materials get depleted over time. Fluxes of source beams are read from an ion gauge and recorded as Beam Equivalent Pressure (BEP). A direct measure of growth rate is performed using RHEED oscillations. Under As rich conditions, deposition of a GaAs layer is enabled by group V adsorption but the growth rate is controlled by group III element[5]. Therefore the time taken to grow 1ML represents the rate at which Ga atoms strike the surface. The RHEED specular spot intensity oscillates during the monolayer growth[5] and the period of oscillation is used to calculate growth rates of elements. Intensity oscillations during a 2-D layer growth is shown in figure 1.3.

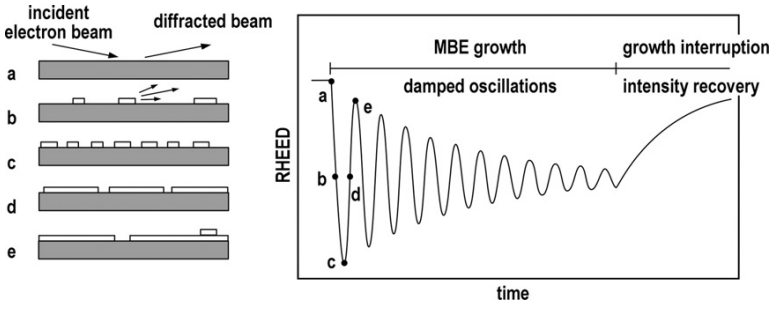

Figure 1.3: Different stages of a monolayer growth mechanism and corresponding intensity of RHEED spot as a function of growth time[1]. (Secondo Franchi, *"Chapter 1 - Molecular beam epitaxy: fundamentals, historical background and future prospects"*, *Molecular Beam Epitaxy*, Oxford, 2013).

Ga and Al growth rates are obtained on a GaAs epilayer grown on a GaAs(001) substrate. A GaAs epilayer of thickness $\sim 0.5 \mu m$ is grown at the oxide desorption

temperature of 580°C[6] (or 20°C -40°C higher) with an As:Ga ratio of 15:1. Growth rate oscillations are measured at the same temperature with an As overpressure. The Ga (or Al) shutter is opened from a few seconds to a minute, to obtain enough oscillations to calculate an average growth rate. After growing an AlAs layer for Al growth rate measurements, a few MLs of GaAs are grown to recover the surface smoothness for subsequent calibration points. Arsenic growth rate measurements can be performed on a Ga-rich surface if necessary. However, the As growth rate is rarely calibrated since in most As related growths, it is only important to maintain a suitably high V/III flux ratio (~15-20). Therefore, only BEP measurements are made of the As beam at different As-valve positions.

In and Sb growth rates measurements are performed on a $\sim 1 \mu m$ thick InSb epilayer grown on a GaAs (001) substrate with an Sb:In ratio of 1.1:1. The epilayer is grown at 380°C and then the substrate temperature is lowered to 25°C less than T_{tr}, where T_{tr} is the temperature at which the surface reconstruction changes from pseudo (1×3) to $c(4 \times 4)$. The In (and Sb) growth rate calibration is comparatively challenging since good oscillations can be obtained only in a narrow window of V/III flux ratio (~1.0-1.1). The In shutter is open for a short time to grow a few MLs of InSb to measure the In growth rate. The Sb growth rate is calibrated from RHEED oscillations in an In-rich background which can be formed by turning off the Sb beam and opening In shutter for a few seconds (8s-10s).

Part II

1.7 Basics of Quantum Structures

A quantum structure is formed when the dimensions of the bulk material is restricted below the de-Broglie wavelength of the carriers in the material along any one or more of the three directions x, y and z. The parameter de-Broglie wavelength, for carriers in a material, is given by the following equation[7]:

$$\lambda = \frac{h}{\sqrt{3m^* k_B T}} \qquad 1.1$$

where, h is Planck's constant, m* is the effective mass of the carrier in material, k_B is the Boltzmann constant and T is the temperature. Values of the de-Broglie wavelength of electrons for GaAs and InP materials at room temperature are 24 nm and 22 nm, respectively. A quantum well (QW) is formed when a lower bandgap material is sandwiched between large-gap materials with a restricted thickness below λ along one direction (z), which is generally the growth direction of a structure. Formation of the QW results in the reduction of the degree of freedom for the charge carriers (electrons and holes) in one direction (z) and hence the carriers become confined in the well. A quantum wire or a quantum dot is formed when the thickness of material is restricted below λ along two directions (z, y) or along all the three directions (x, y, z), respectively. Figure 1.4 shows schematic representation of bulk and quantum structures[7].

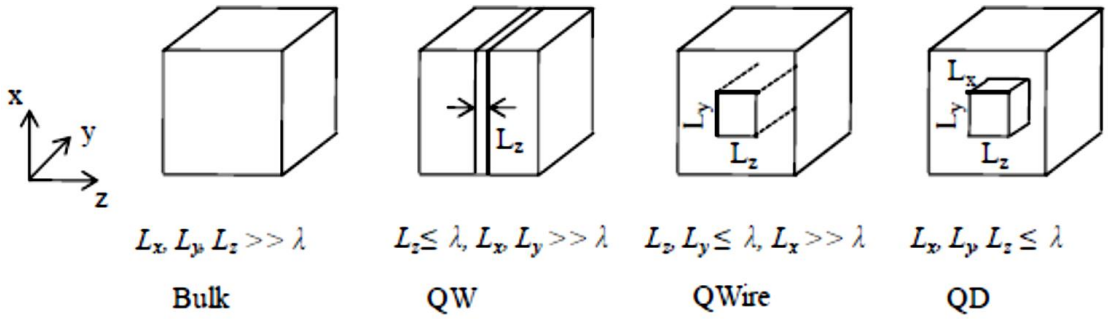

Figure 1.4: Schematic of bulk and quantum structures. (M. Grundmann et al., *Quantum Dot Heterostructures*, John Wiley and Sons, 1999).

The energy of the confined carriers in a QW is given by[8, 9]:

$$E(n_z, k_{x,} k_y) = E_{n_z} + \frac{\hbar^2}{2m^*_{e,h}}(k_x^2 + k_y^2) \qquad 1.2$$

where E_n is the n^{th} quantized eigen energy value of the z-component of the Hamiltonian, $\hbar$ is Planck's constant, $m^*_{e,h}$ is the effective mass of electron or hole, and k_x, k_y are the components of the carrier wavevector along the directions where the motion of electron or hole is free. Schematic representation of equation 1.2 is shown in figure 1.5[8]. The values of E_n are denoted by E_1, E_2 for electrons; by E_1(HH), E_2(HH) for heavy holes; and by E_1(LH), E_1(LH)for light holes. Since there is no allowed energy value below E_1 for electrons, the resultant lowest bandgap in a QW increases from its bulk value of E_g to an amount of E_1+ E_1(HH).

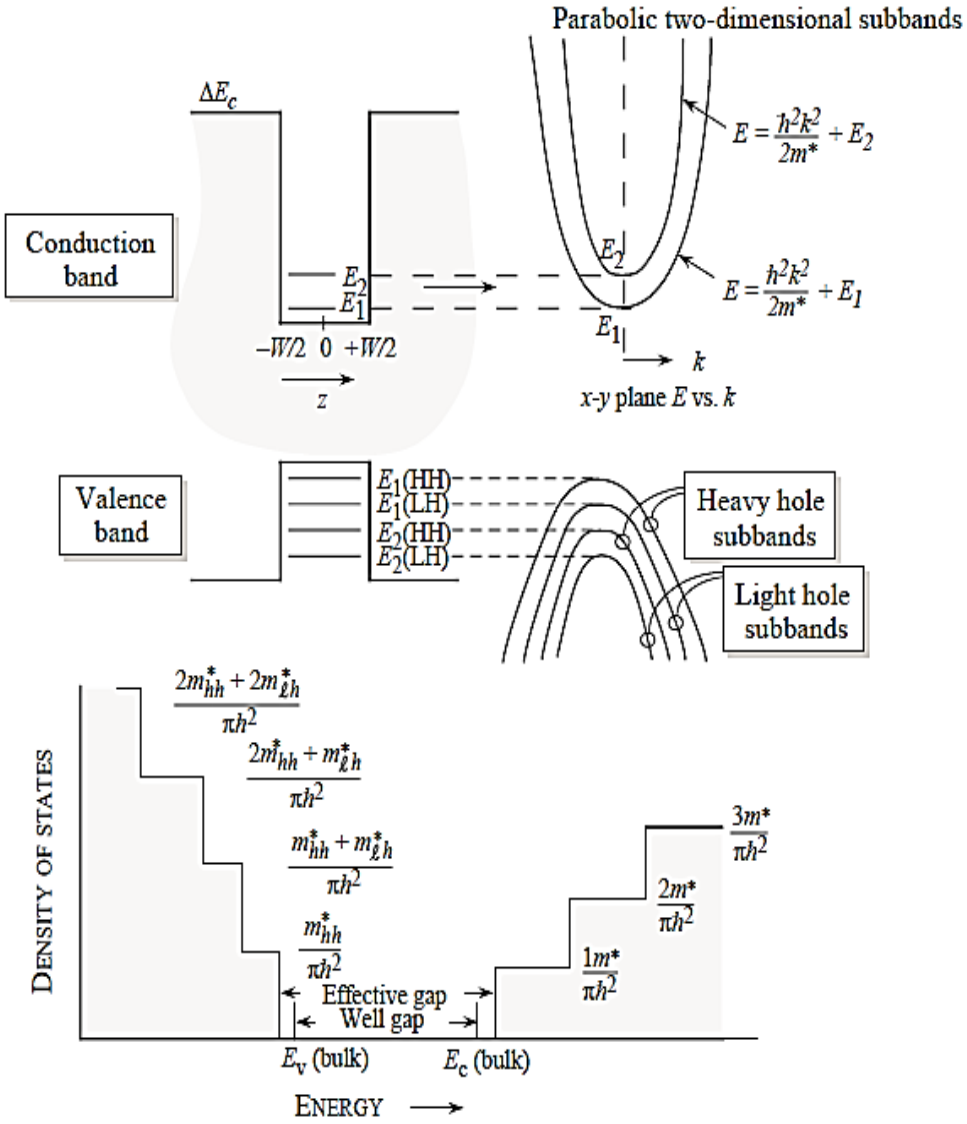

Figure 1.5: Band diagram of QW structure with confined energy levels of system, along with DOS of a 2D system. Conductions and valence band are discontinuous along the growth direction. Parabolic subbands are produced in the conduction band and the valence band. (J. Singh, *Electronic and Optoelectronic Properties of Semiconductor Structures*, Cambridge Uiversity Press, 2003).

In a MQW, the thickness of the barrier layer between two adjacent QWs is sufficiently large such that the electronic wave functions of individual QWs do not overlap.

However, if the barrier thickness between the QWs is relatively thin so that there is sufficient overlap of the electronic wave functions of individual QWs, then the energy level splits and forms a miniband. Such a MQW structure with overlapping wavefunctions is referred to as a superlattice (SL). In a SL, a periodic structure is artificially created by repeatedly growing the QW structure several times, with thin enough barriers to allow coupling(tunneling through barriers) of wells. A MQW and SL structure along with the bandstructure and electronic wavefunction are depicted in figure 1.6. Miniband formation and tuning of energy levels is further described in chapter 5, section 5.4.

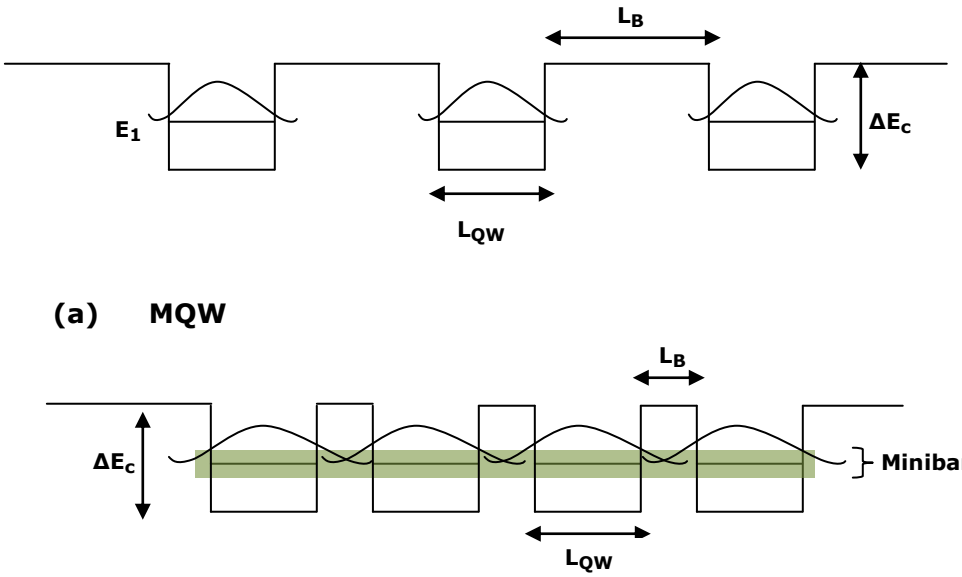

Figure 1.6: Schematics of a (a) multiple quantum well and (b) superlattice structure, E_1 is the confined electronic energy level of the QW. Formation of minbands from the energy levels of the corresponding single quantum well is shown. The SL structure forms an artificial one-dimensional crystal with period (L_B + L_W), where L_B and L_W represent the thickness of the QW and barrier regions respectively. The width of the minibands depends on the strength of the coupling through the barriers.

One advantage of a quantum structure over its bulk counterpart is the tunability of energy levels over a wide range by changing the size of the quantum structure and composition of the barrier material. Also, the density of states (DOS), defined as the number of electronic states per unit energy range per unit area (2D) or volume (3D), for the quantum structure is drastically different than that of the bulk structure. Figure 1.7 depicts the DOS for bulk, QW and SL quantum structures[8, 10, 11]. For 3D bulk, the DOS is continuous and proportional to the square root of energy whereas for a QW it has a step like behavior starting at E_1 with a value $m^*/\pi\hbar^2$ that does not change until the second subband appears at E_2, where it jumps by $m^*/\pi\hbar^2$. The sharp step rise of the DOS observed in a QW is smoothed out in the superlattice structure due to the miniband formation[10,11,12]. The modified DOS offers several advantages of the quantum structures that have been utilized in high speed electronics, optical and solar cell applications.

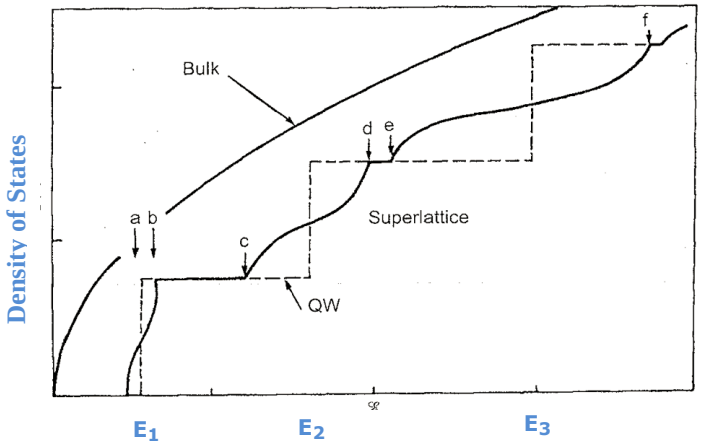

Figure 1.7: Schematics of DOS for 3D bulk, and 2D quantum structures.
(Kelly, *Low-Dimensional Semiconductors*, Oxford University Press, 1995)

Chapter 2: Post Growth Characterization Techniques

2.1 Introduction

Characterization techniques play an important role in the assessment and quality improvement of semiconductor structures. Various characterization techniques are routinely performed on MBE grown structures to determine their physical and electrical properties. Epitaxial structures described in this dissertation were characterized using Scanning Electron Microscopy (SEM), High resolution X-ray diffraction (HRXRD), Hall Effect Measurements, and Photoluminescence (PL) Spectroscopy. This chapter describes HRXRD and Hall Effect experimental procedures in detail and the basic principles of SEM and PL spectroscopy.

2.2 Surface Characterization-Scanning Electron Microscopy

Scanning electron microscope (SEM) is a non-destructive imaging technique in which accelerated(high-energy) electrons are finely focused on a specimen and the variety of signals produced as the electrons decelerate into the sample are collected to examine characteristics of the sample(surface topography, composition, etc.). These signals include secondary electrons, backscattered electrons (BSE), diffracted backscattered electrons, characteristic X-rays, visible light (cathodoluminescence), and heat. Secondary electrons and backscattered electrons are commonly used for imaging samples: secondary electrons (low energy electrons due to inelastic collision between the primary beam and the loosely bound conduction or tightly bound valence electrons

of the specimen) are the most useful for showing morphology and topography on samples.

Subsytems of the SEM and their functions

Major components of a SEM are the electron column (figure 2.1), and the electronics console which consists of a CRT screen and controls for the electron beam. A brief description on SEM subsystems and their functions are given below[13,14].

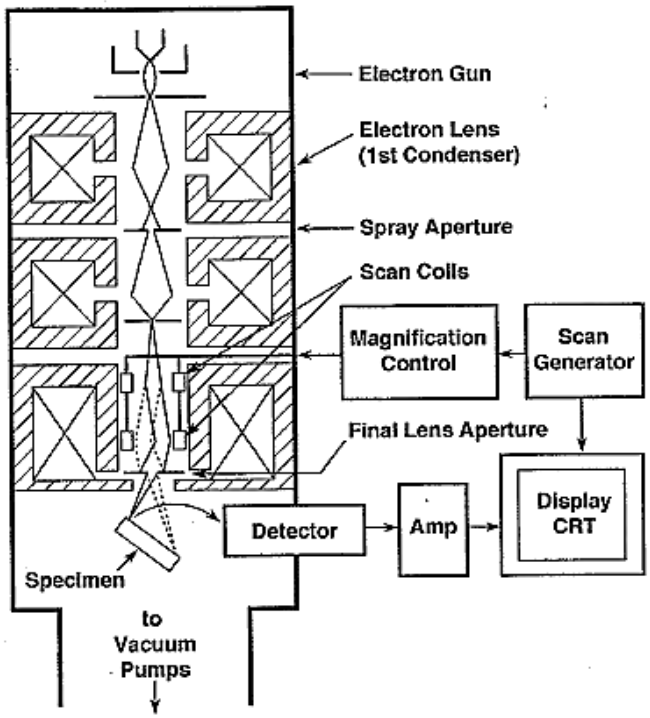

Figure 2.1: Schematic of the electron column showing the electron gun, lenses, the deflection system, and the electron detector. (Goldstein et al., *Scanning Electron Microscopy and X-ray Microanalysis*, Springer, 2003).

(a) Electron gun: Consists of three components- a Tungsten wire filament serving as negative electrode, the grid cap or Wehnelt (control electrode), and the positive electrode. These are all connected to appropriate high-voltage supplies.

Electrons are emitted from a thermionically heated filament, focused by a grid cap which is slightly more negative than the cathode, and accelerated towards the anode which is connected to the ground potential (0V).

(b) Condenser lenses: Electromagnetic lenses are responsible for converging the beam that passes through from an initial beam size of ~50μm down to a ~10nm spot size on the specimen by changing the current (and therefore the magnetic field across the lens) running through an enclosed coil of wire. These are responsible for demagnifying the beam and determining its intensity when it strikes the sample. The beam is condensed by a first condenser lens usually controlled by the "coarse probe current knob" and a second condenser lens controlled by a "fine probe current knob".

(c) Apertures: The function of the aperture is to constrict extraneous electrons. The final lens aperture located below the scanning coils determines the diameter of the beam spot striking the specimen.

(d) Scanning system: Deflects the beam across the sample in a grid type scanning, dwelling on points for a certain time set by the scanning speed.

(e) Final (Objective lens): Focuses the beam on the desired area of the sample. An astigmatism corrector is located in the objective lens to correct an elliptical beam into one with a circular cross section.

(f) Electron detector: Electrons emitted after the sample- primary beam interaction are collected by a standard Everhart-Thornley detector. A positively charged collector screen captures SE and BSE signal from the scan. An image is formed when the signal collected from each point varies from one another. The

electronics of the detector system converts the point-to-point intensity variation into an image.

(g) Vacuum system: The SEM is typically equipped with a roughing pump and a turbo-molecular pump to obtain a vacum of ~10^{-6} Torr. A high vacuum is required to prevent oxidation of the hot tungsten filament in the presence of air, for proper function of the column optics and to reduce the loss of beam electrons due to interactions with air and dust.

Surface images of samples described in this dissertation were obtained with a Zeiss 960 conventional SEM and JEOL JSM-880 medium-high resolution SEM located at the Samuel Roberts Noble Microscopy Laboratory, University of Oklahoma.

2.3 Structural Characterization-HRXRD (High Resolution X- Ray Diffraction)

High resolution x-ray diffraction is a non-destructive, relatively fast characterization technique widely used to determine lattice parameters, layer thickness, lattice mismatch, strain and composition of the MBE grown single-layer or multi-layer epitaxial films.

2.3.1 Experimental setup

Diffraction measurements were carried out using a Philips Materials Research Diffractometer with a CuKα_1 source that produces a monochromatic x-ray beam with a wavelength (λ) of 1.5406Å. The beam is incident from a four-reflection Ge (220) monochromator and generated with an initial power of 1200W. The experimental arrangement of an x-ray diffractometer is shown in figure 2.2.

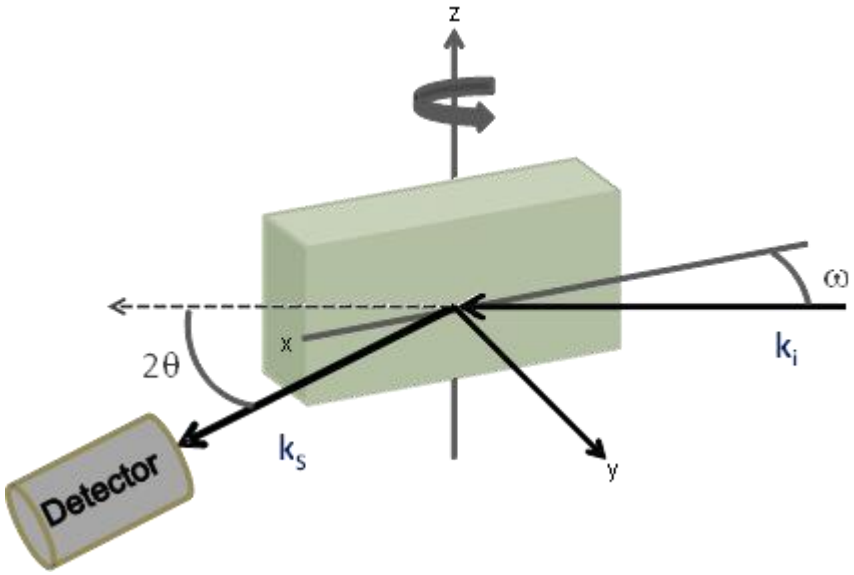

Figure 2.2: Schematic of x-ray diffraction measurement setup. The sample is mounted on a cradle, known as the goniometer, which provides x y, and z linear motions and rotation (ϕ) and tilt (ψ) angles. The beam is incident at angle ω and the diffracted beam is collected at an angle 2θ, relative to the incident beam.

The beam is incident at an angle ω (the angle between the source and the sample surface), and the diffracted beam is received by the detector positioned at 2θ (the angle between the incident beam and the detector). The goniometer with the sample and the detector are motorized to move to selected angular positions, with respect to the sample surface, ω and 2θ. The goniometer can also rotate about the y-axis (ϕ angle) and x-axis (ψ-tilt angle) to optimize reflections from crystalline planes.

2.3.2 Scattering geometries

For parallel planes of atoms, with d_{hkl} spacing between them, constructive interference occurs only when Bragg's law is satisfied ($2d\sin\theta=n\lambda$). In an x-ray diffraction

measurement, the family of planes (hkl) chosen to perform the scan with, produces a diffraction peak only at a specific angle θ from which the interplanar distance can be determined. Two common scanning geometries are symmetric, in which the planes (or sample) are normal to the diffracting vector **S** and asymmetric, in which the planes (or sample) is tilted with respect to the diffraction vector (figure 2.3).

Symmetric scans provide information such as out-of-plane lattice constant c, strain component $\varepsilon^{\perp}$ and the layer thickness. Using asymmetric scans, lattice constants both perpendicular and parallel to the surface, and in-plane strain can be calculated.

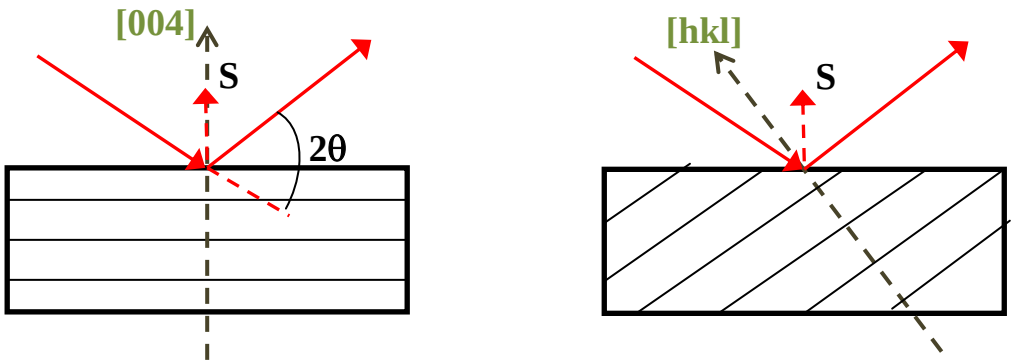

Figure 2.3: Schematic of symmetric and asymmetric geometries

2.3.3 Scan modes

Two main scan modes, rocking curve scan (ω-scan) and coupled scan (ω-2θ) are used to probe for diffraction peaks that satisfy Bragg condition. In a rocking curve, the detector is set at a specific $2\theta_B$ position, where θ_B is the Bragg angle, and the sample angle ω is rocked around the Bragg peak slightly. In a coupled scan, the 2θ position of the detector is also changed, in a coupled manner with ω so that the direction being measured does not change (diffraction vector S does not change). A sharp peak will be

observed only when crystallographic direction (normal to the surface) is parallel to the diffraction vector S. Angular optimization of ϕ and ψ are performed on the substrate peak to bring the diffraction vector and the crystallographic direction into alignment and obtain maximum intensity. The ψ angle optimization is sufficient for the symmetric scan but asymmetric scans require both ϕ and ψ angle optimizations to enhance diffraction features. Once the alignment procedure is completed, ω or ω-2θ scans can be performed for the desired (hkl) reflection.

2.3.4 Determination of lattice parameters and alloy composition

From the equation for the interplanar spacing in tetragonal crystals[15],

$$\frac{1}{d_{hkl}^2} = \frac{h^2+k^2}{a^2} + \frac{l^2}{c^2} \qquad 2.11$$

and, the following relationship for Bragg's law is obtained:

$$\frac{4\,sin^2\,\theta_l}{\lambda^2} = \frac{h^2+k^2}{a^2} + \frac{l^2}{c^2} \qquad 2.12$$

For the 001 crystal surface, the plane tilt angle φ can be written as:

$$sec^2\,\varphi = \frac{c^2}{l^2}\left\{\frac{h^2+k^2}{a^2} + \frac{l^2}{c^2}\right\} \qquad 2.13$$

By solving the above equations, the out-of-plane lattice constant c and the in-plane lattice constant a can be obtained:

$$c = \frac{l\lambda}{2\sin\theta\,cos\varphi} \qquad 2.14$$

$$a = \frac{l\lambda}{2\sin\theta}\sqrt{\frac{h^2+k^2}{l^2}} \qquad 2.15$$

If the peak separation is $\Delta\omega_1$ and $\Delta\omega_2$ at incident geometries ω^- and ω^+ respectively, then the Bragg angle difference $\Delta\theta$ between the layer and the substrate is given by its average[16],

$$\Delta\theta = \frac{\Delta\omega_1 + \Delta\omega_2}{2} \qquad 2.16$$

The tilt between the layer and the substrate $\Delta\varphi$ is half the difference of the two peak separations[16]:

$$\Delta\varphi = \frac{\Delta\omega_1 - \Delta\omega_2}{2} \qquad 2.17$$

The tilt of the layer φ from (001) surface is directly calculated from half the difference of the two peak positions ω^- (*hkl*) and ω^+ (*-h-kl*) [17].

$$\varphi = \frac{\omega_2 - \omega_1}{2} \qquad 2.18$$

Calculation of alloy composition of $AlAs_xSb_{1-x}$ grown on GaAs (001):

Samples described in this dissertation include structures grown on both lattice matched and mismatched substrates. Growth on a highly mismatched substrate can result in a strained or partially relaxed epilayer. Strain relaxation leads to misfit dislocations which originate at the layer-substrate-interface resulting in tilted lattice cells[18]. Therefore, in general, it is more accurate to derive the alloy composition is derived from asymmetric reflections when the layer is partially relaxed. On the other hand, calculations from symmetric reflections assume the layer to be fully relaxed. For the $AlAs_xSb_{1-x}$ layers presented in this dissertation, the ratio of the group-V constituents in the alloy are

calculated from symmetric (004) reflections. In this case, ω^- and ω^+ correspond to ϕ=0° and ϕ=180°, respectively, and $\varphi=\Delta\varphi$. The corrected experimental Bragg angle for the layer is the difference between the theoretical substrate Bragg angle and the experimental peak separation. This can be written as:

$$\theta = \theta_S - \Delta\theta \qquad 2.19$$

where θ_S (=33.024°) is the theoretical Bragg angle for the GaAs(004) substrate reflection and can be calculated by setting h=0, k=0, l=4, λ=1.5406Å and c=a= 5.65325Å in the formula for lattice constants. A diffraction intensity profile for a 500nm thick $AlAs_xSb_{1-x}$ epilayer grown on GaAs (001) is shown in figure 2.4. The measured XRD data and calculated lattice parameters for this sample are given in table 2.1. The out-of-plane lattice constant for this sample is calculated to be 6.0656 Å.

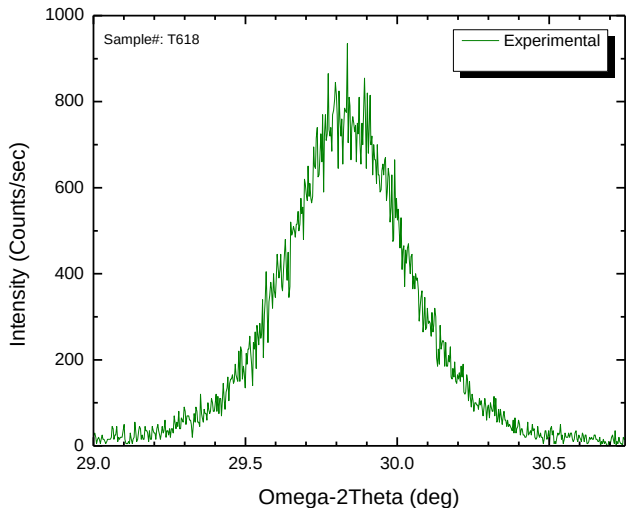

Figure 2.4: (004) ω-2θ intensity profile of 500nm $AlAs_xSb_{1-x}$ epilayer grown on GaAs (001) substrate. The out-of-plane lattice constant for this sample is calculated to be 6.0656 Å.

T618	**Substrate (GaAs)**			**Epilayer ($AlAs_xSb_{1-x}$)**					
h k l	θ_S (theor.)	ω^- (ϕ=0°)	ω^+ (ϕ=180°)	ω^- (ϕ=0°)	ω^+ (ϕ=180°)	$\Delta\theta_{avg}$	$\Delta\varphi$	θ_B $=\theta_S - \Delta\theta$	c (Å)
0 0 4	33.024	33.118	32.336	30.599	29.844	2.5055	0.039	30.5185	6.0656
Peak separation $\Delta\theta$				2.519	2.492				

Table 2.1: X-ray diffraction data obtained from (004) reflections and calculated lattice parameters for $AlAs_xSb_{1-x}$ grown on GaAs (001) substrate (sample T618).

The percentage of AlAs and AlSb in the $AlAs_xSb_{1-x}$ alloy is calculated using Vegard's law. Vegard's law is an approximate empirical rule which states that a linear relationship exists between the lattice constant of an alloy and the concentrations of the constituent elements. Vegard's expression for a binary compound can be written as:

$$a_L(x) = xa_A + (1-x)a_B \ , \qquad x = \frac{a_L - a_B}{a_A - a_B} \tag{2.20}$$

$$x_{AlAsSb} = \frac{a_L - a_{AlAs}}{a_{AlSb} - a_{AlAs}}, \qquad x = \frac{6.0656 - 5.6605}{6.1355 - 5.6605} = 0.853$$

The calculated Sb percentage in $AlAs_xSb_{1-x}$ is 85.3%. The As:Sb ratio in the alloy is 15:85. This is a close value to the intended composition.

The mismatch *m* of a heteroepitaxial layer is defined by[16]:

$$m = \frac{a_L - a_S}{a_S} \tag{2.21}$$

where a_L and a_S are the bulk lattice parameters of the cubic form layer and substrate, respectively.

The perpendicular mismatch m_p is defined by:

$$m_p = \frac{c_L - a_s}{a_s} \qquad 2.22$$

where c_L is the out-of-plane lattice spacing of the layer.

The fully strained layer mismatch *m* is related to m_p by:

$$m = \frac{1-v}{1-v} m_p \qquad 2.23$$

where *v* (0.33 for most materials*)* is the Poisson ratio of the layer material. If the layer is fully relaxed the layer unit cell is cubic and *m* is equal to m_p .

2.3.5 Determination of superlattice periods and thickness

Superlattice structures consist of periodic layers (ABAB…, etc.) of different composition which results in many identical interfaces. The intensity contribution from these identical interfaces of a superlattice consists of two components:

1. Bragg reflections from the A and B components of the SL. This is the zero-order or average mismatch peak from which the average composition of the A+B layers may be obtained. This peak can overlap or appear closer to the substrate peak. A shifted peak indicates strain or change in stoichiometry.
2. A set of satellite peaks symmetrically surrounding the zero-order peak, with mean period of repeated unit determined by the periodicity d :

$$d = \frac{(n_1 - n_2)\lambda}{2(sin\theta_1 - sin\theta_2)} \qquad 2.22$$

Satellite peak features can be used to study thickness of the SL unit and the sharpness of the interfaces.

2.4 Electrical Measurement- Hall Effect

The classical Hall Effect measurement is one of the most common electrical characterization techniques to measure electrical transport properties such as resistivity, carrier density, carrier type and the mobility of semiconductor structures.

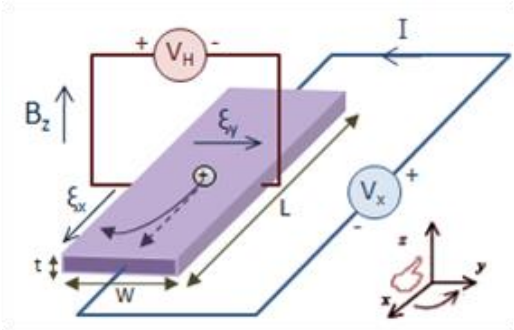

Figure 2.5: Hall Effect experimental setup and carrier motion for holes.

Figure 2.5 shows the Hall experimental setup [19]. When a magnetic field is applied to a conductor perpendicular to the current flow direction, it produces a Lorentz force perpendicular to the magnetic field and the current. Carriers are deflected to an edge until steady state is reached when the Lorentz force on carriers is balanced by the force of the electric field due to carriers at the edges. This is known as the Hall Effect and the voltage drop perpendicular to the current direction is called the Hall voltage.

Assuming motion in x and y directions, the equation of motion for the electrons at the steady state is given by[20]:

$$-e(\boldsymbol{E}+\boldsymbol{v_d}\times\boldsymbol{B})=\frac{m\boldsymbol{v_d}}{\tau} \quad 2.23$$

This can be written in the tensor form:

$$\begin{bmatrix}E_x\\E_y\end{bmatrix}=\begin{bmatrix}\frac{m}{e\tau} & -B\\ B & \frac{m}{e\tau}\end{bmatrix}\begin{bmatrix}v_x\\v_y\end{bmatrix}, \quad 2.24$$

By using $\boldsymbol{j}$=-ne$\boldsymbol{v_d}$ and μ=eτ/m (from results of the Drude model approximation), equation 2.24 can be rewritten in the form:

$$\begin{bmatrix}E_x\\E_y\end{bmatrix}=\sigma^{-1}\begin{bmatrix}1 & -\mu B\\ \mu B & 1\end{bmatrix}\begin{bmatrix}j_x\\j_y\end{bmatrix}, \quad 2.25$$

where, σ=enμ is the conductivity when B=0..

The resistivity tensor also in the same form is:

$$\begin{bmatrix}E_x\\E_y\end{bmatrix}=\begin{bmatrix}\rho_{xx} & \rho_{xy}\\ \rho_{yx} & \rho_{yy}\end{bmatrix}\begin{bmatrix}j_x\\j_y\end{bmatrix} \quad 2.26$$

Where the, longitudinal resistivity is $\rho_{xx}=\frac{1}{\sigma}=\frac{1}{en\mu}$ 2.27

And the transverse resistivity(or Hall resistivity) is $\rho_{xy}=-\rho_{yx}=-\frac{1}{en}B$ 2.28

The Hall resistivity linearly increases with B in the low field limit. R_H= -1/en is known as the Hall coefficient. R_H has opposite polarities for n and p type carriers; therefore from the sign of the measured R_H, the dominant carrier type of the structure can be determined.

At steady state, setting the transverse current j_y=0 to zero in equation 2.26 gives,

$$E_x=\rho_{xx}j_x\ ;\quad E_y=\rho_{yx}j_x \quad 2.29$$

From equation 2.28 and 2.29, the transverse resistivity is given by:

$$\rho_{xy}=\frac{V_H}{I}=-\frac{1}{en_s}B \quad 2.30$$

where V_H is the transverse voltage drop, I is the current passing through the sample and n_s is the sheet carrier density. The experimental procedure of the Hall technique and determination of electrical properties of the sample (n_s, ρ_{xx} and μ) are briefly described below.

Measurements

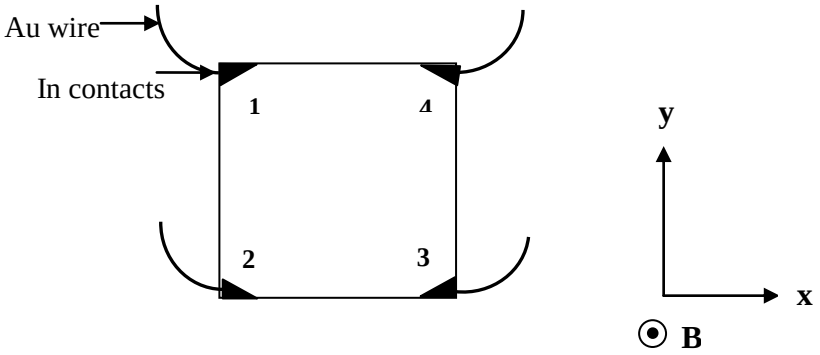

Figure 2.6: The Van der Pauw square sample configuration used for Hall measurements.

The Hall measurement is performed on a van der Pauw square specimen[21], cleaved from the MBE grown wafer, to determine the sheet carrier density, the resistivity and the mobility of the sample. The measurement configuration is shown in figure 2.6. Pure In was applied at the corners of the sample for ohmic contacts. Temperature-dependent Hall measurements were done in a closed-cycle He refrigerator from 300K to 20K.

Hall resistivity ρ_{xy} linearly increases with B in the low field limit. Therefore, in low field conditions, the sheet carrier density can be determined from the Hall coefficient (R_H)-the slope of transverse resistivity versus B field:

$$n_s = -\frac{1}{e}\frac{1}{\left(\frac{d\rho_{xy}}{dB}\right)} \quad 2.31$$

Typically, V_H is measured when the magnetic field strength is swept through 0 to 0.14T at constant current. V_H is the transverse voltage drop measured between contacts 2 and 4 (V_{24}) when I is passed between 3 and 1 (I_{31}) with the magnetic field applied perpendicular to the surface. R_H is negative (or positive slope) for electrons and positive (or negative slope) for holes.

From equation 2.29 the longitudinal resistivity (or sheet resistivity), at B=0 is given by:

$$\rho_{xx} = \frac{V_x}{I}$$

The longitudinal resistivity or the sheet resistivity of the sample is measured according to the van der Pauw geometry with **B**=0. For a sample homogenous in thickness and carrier density, and very large in comparison to the point-like contacts which are placed at the boundaries, the longitudinal resistivity is given by the van der Pauw formula:

$$\rho_{xx} = \frac{\pi}{ln2}\left[\frac{R_{12,43}+R_{43,12}+R_{23,14}+R_{14,23}}{4}\right] f\left[\frac{R_{12,43}+R_{43,12}}{R_{23,14}+R_{14,23}}\right] \quad 2.32$$

where, $R_{12,43}$ is the four point resistance and given by;

$$R_{12,43} = \frac{V_{12}}{I_{43}},$$

and *f* is the correction term for the arbitrary shape of the sample. V_{12} is the dc voltage drop between contacts 1 and 2 when the current *I* is passed from contact 4 to 3. Other four point resistances are defined similarly. For a square sample with small contacts, *f* is 1. Then the longitudinal resistance can be written as;

$$\rho_{xx} = \frac{\pi}{ln2} R_{av} \text{ , where, } R_{av} = \left[\frac{R_{12,43}+R_{43,12}+R_{23,14}+R_{14,23}}{4}\right] \quad 2.33$$

Mobility is calculated using the ρ_{xx} at B=0 (equation 2.27) and the carrier density n_s:

$$\mu = \frac{1}{en_s\rho_{xx}} \qquad 2.34$$

2.5 Optical Properties- Photoluminescence Spectroscopy

Photoluminescence (PL) is a simple but important technique for investigating optical responses from bulk or quantum structures. In a PL measurement, the sample is optically excited by a pump beam, usually a laser light with photon energy greater than the band gap of the semiconductor sample, which generates electron-hole pairs that radiatively recombine to emit light. The energy distribution of the emitted photon is measured and analyzed to determine the confined energy levels (figure 2.8) of the sample. To obtain maximum spectroscopic information, it is necessary to cool the sample to cryogenic temperatures to minimize thermally activated non-radiative recombination processes and thermal line broadening. A typical PL system (figure 2.7) consists of an excitation source (for most III-V semiconductors, the source is an argon-ion laser delivering 0-15mW power at 5145 Å), a cryostat and sample holder assembly, a high-resolution scanning spectrometer, and a detection system[22]. Usually this technique provides information about the lowest transitions in quantum structures.

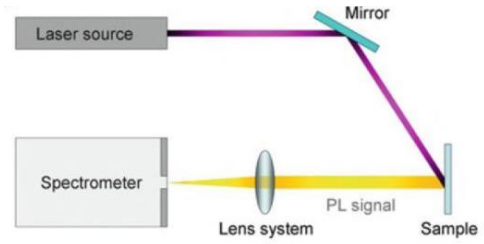

Figure 2.7: Schematic of photoluminescence arrangement. (Challa S.S.R. Kumar, *UV-VIS and Photoluminescence Spectroscopy for Nanomaterials Characterization*. Springer, 2013).

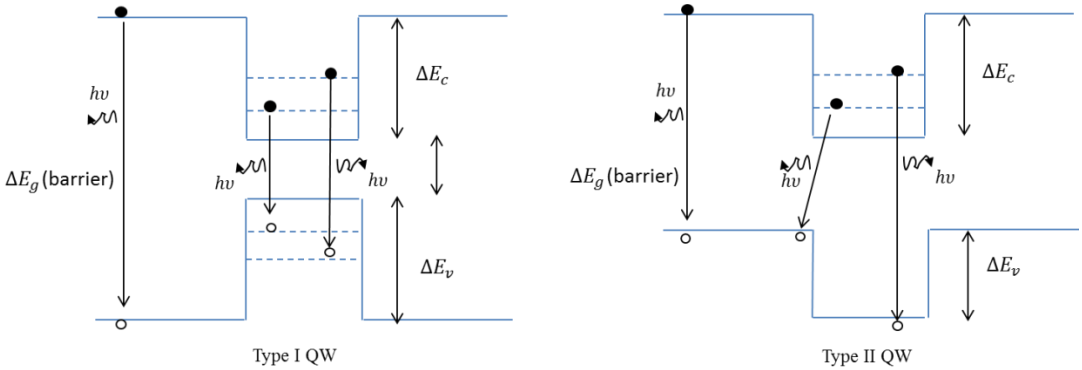

Figure 2.8: Illustration of photoluminescence process in type I and type II quantum wells. Different transitions, spatially direct and indirect, between confined levels of electrons and holes can be observed in PL experiments of a type-I and type-II QW structure.

The PL measurement system at OU is equipped with excitation wavelengths of 632.8nm (red HeNe) and 442nm (blue HeCd). A liquid N_2 cooled InGaAs linear photodiode array used as the detector has a detection range 900nm- 1700nm. For low temperature measurements, the sample is either cooled using a flow cryo-stat or closed cycle He cryo-stat.

Chapter 3: Doping Limitations in Uniformly Doped $In_xGa_{1-x}As$

3.1 Introduction

Complementary Metal-Oxide Semiconductor (CMOS) inverters are the heart of the current semiconductor industry which is continuously driven towards higher performance (ultrafast computation, multiple functionality, low standby power and operating power, etc). A CMOS inverter consists of both n-type and p-type transistors with high mobility carriers. Si based transistors are used in the CMOS circuits until now because of their physical properties (comparable electron and hole mobilities) and well-established fabrication techniques. III-V narrow gap materials are of interest as a successor due to their high electron mobilities[23]. However, their low hole mobilities for p-channels, lack of a native oxide and integration difficulty on Si substrates[23] are the main roadblocks for their entry in CMOS applications. There are ongoing efforts to integrate high-k dielectric material with III-V devices[24,25,26].

Source and drain regions in a FET need to be highly doped for low contact resistance. We investigated doping efficiency at higher concentrations in p-type and n-type $In_xGa_{1-x}As$ for the source and drain regions of $In_xGa_{1-x}As$ based FETs. Growth quality degradation is a commonly reported issue at high doping concentrations in InGaAs. This project was sponsored by Intel Corp with the goal of achieving high quality samples with concentrations ranging from $3\times10^{19}cm^{-3}$ to $5\times10^{19}cm^{-3}$.

3.2 MBE Growth of Doped $In_xGa_{1-x}As/In_yAl_{1-y}As$ Layers

The electron or hole concentration of a semiconductor can be manipulated by adding specific dopant atoms to a pure semiconductor. In our system, Si and Be sources are routinely used as the n-type and p-type dopants, respectively. When the column IV Si atom substitutes for a column III element like In or Ga, the fourth valence electron of the Si atom that does not fit into the bonding structure becomes weakly bound to the donor site. This electron becomes a conduction band electron that is free to move once it is activated from the dopant site. Similarly, the column II Be substitution at the column III sites creates a hole that needs one electron to complete the semiconductor bond. They readily accept an electron from a nearby III-V bond and create a hole that becomes a free carrier in the lattice.

Doped $In_xGa_{1-x}As/In_yAl_{1-y}As$ layers were lattice matched to InP and were grown on a quarter of a semi-insulating InP (001) substrates. The layer structure used throughout the doping studies is shown in figure 3.1. The undoped $In_yAl_{1-y}As$ spacer was grown before the doped $In_xGa_{1-x}As$ as per request from Intel. Si (1110°C $<T_{Si}<$ 1130°C) and Be (870°C $<T_{Be}<$ 1022°C) effusion cells were used to provide n-type and p-type dopants, respectively. The group V As_2 overpressure was 15-20 times higher than the group III beam flux, as measured by an ion gauge at the substrate position. Initial epilayers were grown at a rate 0.63 ML/s and the substrate temperature during growth was 360°C to 500°C. To achieve concentrations above $\sim 3\times10^{19} cm^{-3}$, a lower substrate temperature was required. Layers with maximum concentration were repeated with a lower growth rate.

300nm $In_{0.53}Ga_{0.47}As$(doped)
100nm $In_{0.52}Al_{0.48}As$
SI- InP(001) Substrate

Figure 3.1: 300nm $In_xGa_{1-x}As$ uniformly doped layers were grown on InP(001) substrate to study doping efficiency at high concentrations.

3.3 Hall Characterization Results for Be and Si doped $In_xGa_{1-x}As$

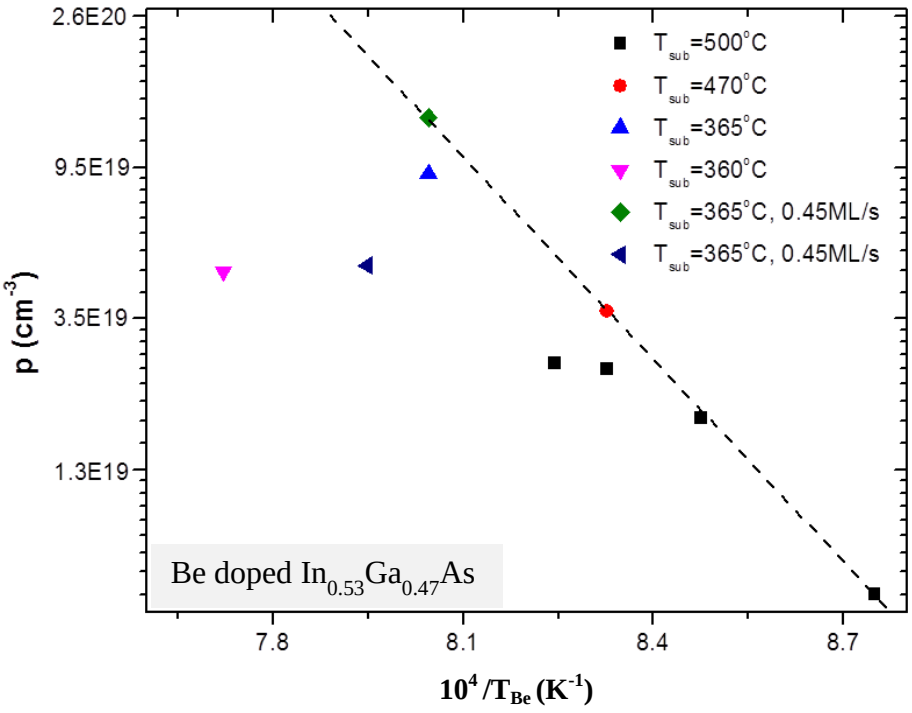

(a)

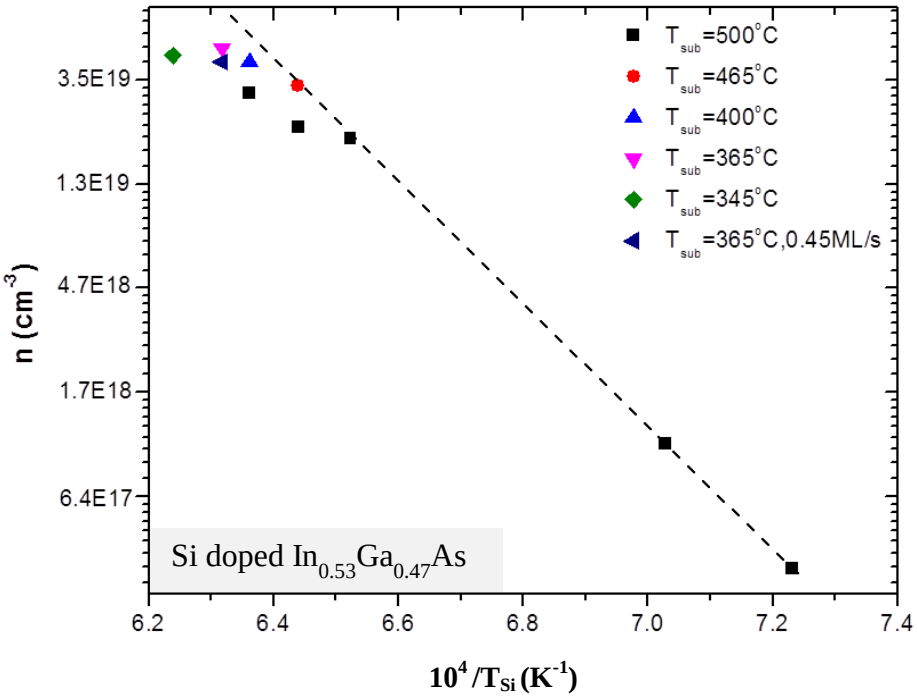

(b)

Figure 3.2: Measured carrier concentration of (a) holes and (b) electrons at room temperature in p-doped and n-doped $In_{0.53}Ga_{0.47}As$ epilayers grown on InP substrates, as a function of Be and Si effusion cell temperature, respectively.

The Hall measurements were performed on ~8mm square pieces in magnetic fields up to 0.14T at room temperature. Measured concentrations, as a function of dopant effusion cell temperature, are shown in figure 3.2. These figures conclude that low concentrations follow an Arrhenius relation and as the doping cell temperature increases, the carrier concentration drops below the Arrhenius projection for both n and p type doping. Optimized growth conditions for an increased efficiency results in agreement with the Arrhenious extrapolation for higher concentrations.

For epilayers grown at 0.63 ML/s with a substrate temperature of 500°C, doping cell temperatures below T_{Si}=1260°C (T_{Be}=907°C) resulted in electron (hole) concentrations that followed an Arrhenius relation with an activation energy of 5.0 eV (4.0 eV). At higher cell temperatures, the carrier concentration saturated at approximately $n=3.1\times10^{19}cm^{-3}$ ($p=2.6\times10^{19}cm^{-3}$). For T_{Si}=1300°C (T_{Be}=928°C), the carrier concentration was increased to $n=4.2\times10^{19}cm^{-3}$ ($p=3.3\times10^{19}cm^{-3}$) through use of a lower substrate temperature of 400°C (470°C). The maximum carrier concentration achieved through lowering the substrate temperature was $n=4.8\times10^{19}cm^{-3}$ ($p=9.1\times10^{19}cm^{-3}$). For Be doping, the maximum hole concentration was increased to $1.3\times10^{20}cm^{-3}$ by using a lower growth rate.

3.4 Summary of Results and Discussion

Tables 3.1 and 3.2 summarize the growth conditions and the Hall measurements of the maximum concentrations obtained through this doping study. A set of samples were chosen to be studied by SEM and their surface images are shown in figures 3.3 and 3.4.

T_{Be}(°C)	GR(ML/s)	T_{sub}(°C)	p(cm^{-3})	μ(cm^2/V-s)
928	0.63	500	2.5×10^{19}	80
928	0.63	470	3.7×10^{19}(~48%↑)	70
970	0.63	365	9.1×10^{19}	60
970	0.45	365	1.3×10^{20}(~45%↑)	50

Table 3.1: Maximum hole concentrations of p-doped InGaAs at different growth temperatures and growth rates.

T_{Si}(°C)	GR(ML/s)	T_{sub}(°C)	n(cm^{-3})	μ(cm^2/V-s)
1299	0.63	500	3.1×10^{19}	1500
1299	0.63	400	4.2×10^{19}(~35% ↑)	950
1310	0.63	365	4.8×10^{19}	850
1310	0.45	365	4.2×10^{19}	1100

Table 3.2: Maximum electron concentrations of n-doped InGaAs at different growth temperature and lower growth rate.

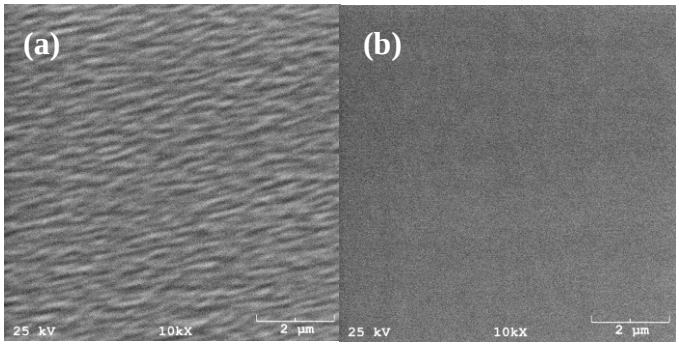

Figure 3.3: Top-view surface SEM images of Be doped InGaAs at different growth temperatures. InGaAs layers were grown at a rate of 0.63 ML/s and doped with Be with T_{Be}= 928°C. Growth temperatures were (a) 500°C and (b) 470°C.

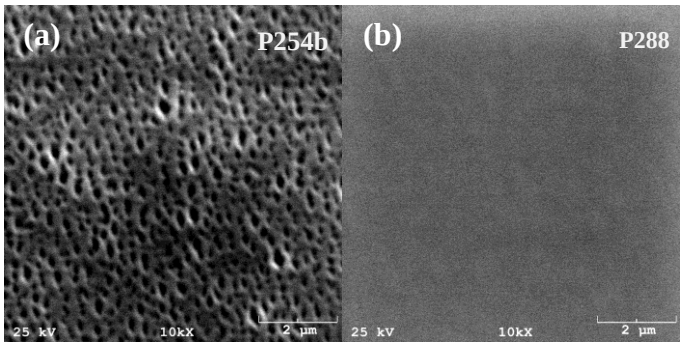

Figure 3.4: Top-view surface SEM images of Si doped InGaAs at different growth temperatures. Epilayers were grown at a rate of 0.63 ML/s and doped with Si with T_{Si}= 1299°C. Growth temperatures were (a) 500°C (P254b) and (b)400°C (P288).

Typically, the growth temperature must be sufficiently high to enable dopants to diffuse on the crystal surface in order to find low energy substitutional sites. However, the

difference in formation energy between the substitutional and interstitial configurations decreases at very high doping concentrations. Incorporation at the preferred substitutional configuration can be achieved by lowering the substrate temperature which reduces the probability of defect formation. Impurity defect formation is proportional to $e^{-\Delta E/kT}$, where ΔE is the difference in the formation energy, k is the Boltzmann constant and T is the substrate temperature[27]. Hall measurements and SEM characterization of the initial heavily doped InGaAs layers grown at an optimized substrate temperature for InGaAs (500°C-550°C) , show inefficient doping and a rough surface which is indicative of the dominating impurity defects (figure 3.3a, figure 3.4a, table 3.1 and 3.2) for samples doped at T_{Si}= 1299°C and T_{Be}= 928°C. An increase in growth quality and dopant incorporation efficiency was observed for a lower growth temperature for these doping cell temperatures (figure 3.3b, figure 3.4b, table 3.1 and 3.2). The highest concentrations were repeated with a lower growth rate which would allow more diffusion time for dopant redistribution to desired substitutional sites.

Be is known to have a high diffusion coefficient towards the surface [28,29,30]. Therefore lowering the growth temperature reduces the interstitial incorporations and the surface diffusion probability. Lowering the growth rate gives more distribution time for substitutional incorporations and thus minimizes surface diffusion probability. Both of these conditions should increase Be incorporation at substitutional sites. A ~ 50% increase in carrier concentration for Be doping was observed in each of these cases (table 3.1). Be doping is ultimately limited by its surface segregation tendency as the concentrations become very high at a certain growth condition. The optimum

temperature and growth rate for Be doping was found to be 365°C and 0.45 ML/s for concentrations in the order of ~$1\times10^{20}cm^{-3}$. The maximum hole concentration achieved with Be doping is $1.3\times10^{20}cm^{-3}$.

For Be doped InGaAs, a concentration of $5.0\times10^{20}cm^{-3}$ has been observed in a gas-source MBE system[33,34]. However, the doping efficiency is observed to be lower in a solid-source MBE system[34], with hole concentrations of $(9\text{-}11)\times10^{19}cm^{-3}$ in heavily Be doped InGaAs[34]. Our results are consistent with these reported values. A hole concentration higher than our current maximum value of $1.3\times10^{20}cm^{-3}$ may be possible with a growth rate slower than 0.45ML/s.

In Si doping, a lower growth temperature allows less interstitial configurations. This is confirmed by a ~ 35% increase in carrier concentration observed for Si doping at a lower growth temperature. However, a lower growth rate does not increase the efficiency (table 3.2). This shows Si incorporation at intended sites is not limited by redistribution time. At high concentrations, Si doping efficiency is assumed to be limited by amphoteric behavior of Si (incorporation at group-V and group-III sites). The optimum temperature and growth rate for Si was found to be 365°C and 0.63ML/s for concentrations in the order ~$5\times10^{19}cm^{-3}$. The maximum electron concentration achieved with Si doping is $4.8\times10^{19}cm^{-3}$.

The reported high Si concentration in InGaAs is $5.0\times10^{19}cm^{-3}$ and $6.1\times10^{19}cm^{-3}$ at 420°C and 370°C respectively[31]. A concentration of $4.0\times10^{19}cm^{-3}$ with degraded

crystalline quality has also been reported[32]. These values are closer to our experimental concentrations. It may be possible to obtain a higher electron concentration by choosing a more optimal growth rate between 0.45 ML/s and 0.63ML/s, and a temperature lower than 365°C for the growth.

It should be noted that the reported concentrations were obtained in experiments carried out in doped InGaAs layers directly grown on InP substrates. There may still be some room to increase efficiency by further optimizing the growth conditions in our investigation. Higher concentrations than the obtained values may be possible in the absence of additional defects that trap dopants formed due to the InGaAs/InAlAs interface quality. Figure 3.5 shows XRD data for the highly Si-doped InGaAs structures shown in figure 3.4a (P254b and P288) which were grown on InAlAs/InP, and for a lightly doped InGaAs structure grown directly on InP (P240). XRD profiles of the highly doped structures do not show a significant difference in structural despite their differences in surface quality. This suggests that the poor doping efficiency could be due to a combination of amphoteric behavior, surface segregation and incorporation at interstitial sites at high densities and growth temperatures in Si doped samples. A sharper peak with higher intensity is observed for the structure with no InAlAs buffer which indicates better crystalline quality. Therefore a higher doping efficiency can be expected for structures grown directly on InGaAs.

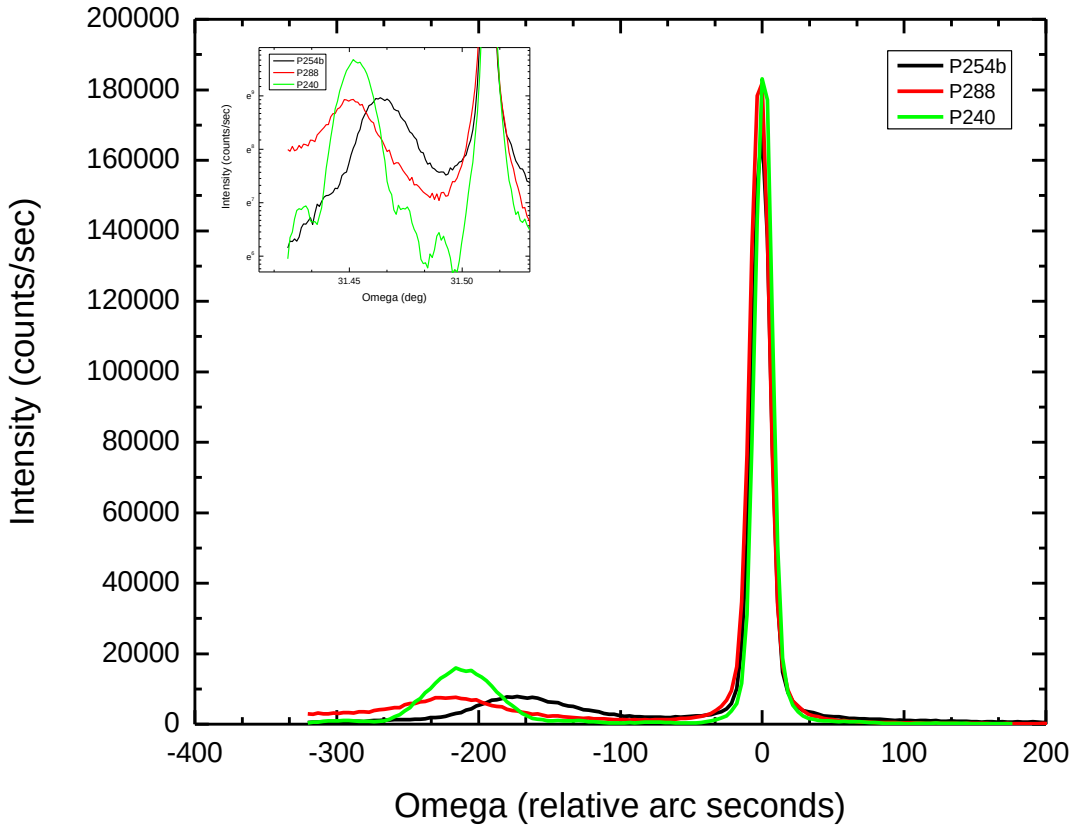

Figure 3.5: (004) diffraction data for InGaAs layers grown on InP(001) substrates, with an InAlAs buffer, highly Si-doped with T_{Si}= 1299°C at (a) a growth temperature of 500°C (P254) and (b) a growth temperature of 400°C (P288) and (c) data for a similar structure but with a lightly doped Si layer and no InAlAs buffer (P240).

Chapter 4: High Density and High Mobility $In_yGa1_{-y}As/In_xAl_{1-x}As$ QW Structures

4.1 Introduction

InGaAs quantum wells (QWs) have been studied for potential transistor applications due to their narrow bandgap (0.75eV for $In_{0.53}Ga_{0.47}As$) and small electron effective mass($0.045m_e$ for $In_{0.53}Ga_{0.47}As$). These properties lead to high intrinsic mobilities. Psuedomorphic InGaAs QWs exhibiting bandgaps of 0.55-0.75eV have been demonstrated and show potential for device applications[23].

Growth of high density(n) and high mobility (μ) $In_yGa_{1-y}As/In_xAl_{1-x}As$ QWs was motivated by their potential for high speed electronic device applications, and ballistic electron studies[35]. High speed applications require high n and high μ at room temperature. Low temperature Aharonov–Bohm (AB) oscillations and other ballistic experiments require a higher path length l which is dependent on μ and the square root of n ($l_e = v_F \tau_E = \hbar k_F/m^* . \mu m^*/e = \mu \hbar k_F/e$, where $k_F = \sqrt{2\pi n}$). In addition to these areas of interest for InGaAs wells with high densities, low density QWs with carrier densities less than $2.0\times10^{11}cm^{-2}$ are used in quantum Hall ferromagnetic experiments.

This chapter describes the growth and characterization of strain-balanced, remotely doped, pseudomorphic $In_yGa_{1-y}As/In_xAl_{1-x}As$ QWs. The $In_{0.64}Ga_{0.36}As$ well is designed to be compressively strained while the $In_{0.45}Al_{0.55}As$ barriers are under tensile strain to

balance the strain in the well-barrier layers. Transport properties are improved by further optimization of the layer structure, doping and growth parameters.

4.2 Simplified Method of Calculating the Electron Density in an *n*-type QW with a Single δ-doping Layer Placed a Distance *d* from the Well

Doping impurities in a conductive layer act as charge scattering centers causing a deterioration of the transport properties at low temperatures. This problem is partially circumvented by placing the dopants by the sides of a QW to spatially separate the ionized impurities from the conductive layer. In order to further separate the ionized dopants from the QW, a spacer layer is inserted between the dopants and the well. Figure 4.1 shows the conduction band profile of a QW with a single δ-doping layer. The electron density dependence on spacer layer thickness is calculated using the model described in this section[36].

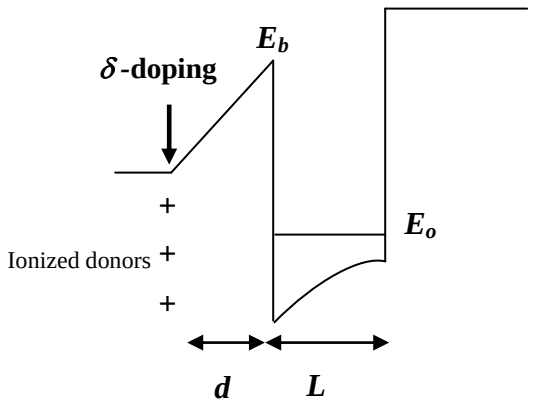

Figure 4.1: Conduction band profile of a QW with a single δ-doping layer.

Assuming single subband occupation at low temperature, the electron density in the well can be obtained from integrating the 2D density of states $D(E) = m^*/\pi\hbar^2$:

$$n = \int_{E_0}^{E_F} \frac{m^*_{edge}}{\pi\hbar^2} dE = \frac{m^*}{\pi\hbar^2}(E_F - E_0) \quad (4.1)$$

where m^* is the in-plane effective mass, E_F is the Fermi level energy, and E_0 is the ground state energy. E_F can be then written as:

$$E_F = \frac{\pi\hbar^2 n}{m^*} + E_0 \quad (4.2)$$

Assuming that the Fermi level at the δ-doped layer is pinned at the donor energy, the electric field in the spacer layer can be described by the equation:

$$\frac{qn}{\varepsilon} = \frac{E_b - E_F - E_A}{qd} \quad (4.3)$$

where q is the charge of the electron, ε is the permittivity of the well material, E_b is the barrier height, E_A is the activation energy of the ionized dopants and d is the spacer layer thickness. Substituting E_F in the above equation and rearranging gives:

$$n = \frac{E_b - E_0 - E_A}{\frac{\pi\hbar^2}{m^*} + \frac{q^2 d}{\varepsilon}} \quad (4.4)$$

Since $E_A << E_b, E_0$, ignoring E_A in the above equation gives the electron density dependence on spacer as:

$$n \approx \frac{E_b - E_0}{\frac{\pi\hbar^2}{m^*} + \frac{q^2 d}{\varepsilon}} \quad (4.5)$$

Values of $\varepsilon = 14\varepsilon_0$ for the permittivity, $m^*_{edge} = 0.045m_0$ for the effective mass, $E_g = 0.814eV$ for the bandgap and $E_b = 0.4eV$ [37, 38] for the barrier height are used in the calculations to determine carrier density n in the well as a function of spacer thickness d. E_0 is estimated as the energy for an infinite potential well of width L.

$$E_0 = \frac{\pi^2 \hbar^2}{2m^* L^2} \tag{4.6}$$

It must be noted that *n* predicted by equation 4.5 depends on spacer thickness only when there are more than enough dopants to provide the predicted number of carriers to the well. In that case, E_F is pinned at E_A by electrons remaining at the dopant layer. When N_d is lower than the predicted *n*, the carrier density can be expected to be independent of spacer thickness and equal to N_d. In addition to the dependence on donor density and spacer thickness, the number of carriers that can be supplied to the well depends on the distance of the δ-doped layer from the surface. Doping farther from the well and closer to the surface can result in carriers providing some electrons to the surface states instead of all supplied electrons reaching the well.

4.3 The Layer Structures of Remotely Doped $In_yGa_{1-y}As/In_xAl_{1-x}As$ QWs

The typical layer structure of a strain balanced, modulation doped, pseudomorphic $In_yGa_{1-y}As/In_xAl_{1-x}As$ QW is shown in figure 4.2. The mobility of the carriers can be manipulated by increasing low band gap content in the well and designing the well to be narrow and deep. Low band gap content in the well (InAs) lowers the effective mass and hence leads to a higher mobility of carriers. A narrow ($L \to 0$) and deep ($V \to 0$) is preferred for one subband occupation to reduce carrier-carrier scattering. The minimum thickness of the well is limited by well-barrier interface scattering. However, the well can be made deeper by increasing the high band gap content in the well (AlAs).

Remotely doped $In_yGa_{1-y}As/In_xAl_{1-x}As$ structures were grown on quarter pieces of semi-insulating 2” diameter InP (001) substrates at or slightly above the oxide

desorption temperature for InP. The growth rates of the strained $In_{0.64}Ga_{0.36}As$ channel and strained $In_{0.45}Al_{0.55}As$ barrier were kept at ~0.53ML/s and ~0.73ML/s, respectively. Lattice matched $In_{0.52}Al_{0.48}As$ barrier layers were grown at a rate of 0.64ML/s. A 15-25 times higher As_2 flux than the group III fluxes, as measured by the beam-flux ion gauge was used during the growth of all the structures.

Since the InP substrates are nearly lattice matched to the $In_{0.64}Ga_{0.36}As/In_{0.45}Al_{0.55}As$ QW structure, a 100nm thick $In_{0.52}Al_{0.48}As$ buffer layer which is lattice matched to InP was grown prior to the QW growth. A 10nm thick $In_{0.64}Ga_{0.36}As$ QW layer was sandwiched between $In_{0.45}Al_{0.55}As$ barrier layers to obtain quantum confinement. A single Si δ-doped layer was placed in the upper $In_{0.45}Al_{0.55}As$ barrier a distance *d* (5-15nm) above the well to provide the electrons to the well. The doping time was varied in conjunction with the upper barrier thickness to obtain high density and high mobility in the well. A second Si δ-doped layer placed in the $In_{0.52}Al_{0.48}As$ layer near the surface provides the electrons required by the surface states. The Si effusion cell temperature was kept at 1170°C during δ-doping, and the 2D density associated with the doping time given in table 4.1. A 10nm $In_{0.53}Ga_{0.47}As$ cap layer was grown on the top to prevent oxidation of the underlying Al containing layer.

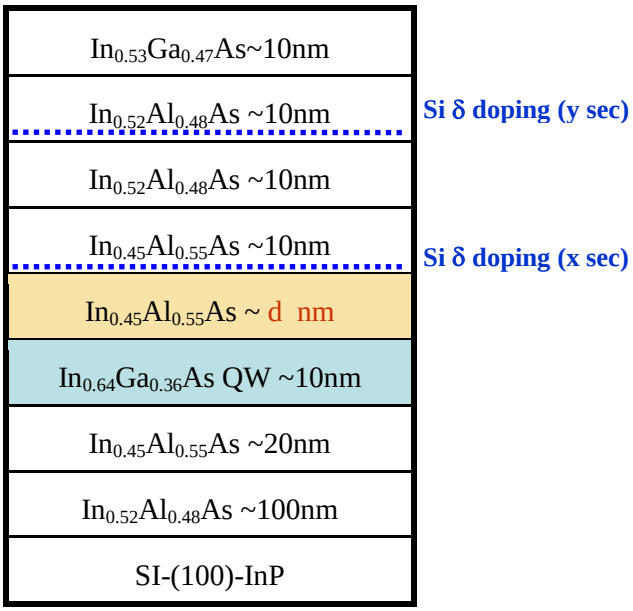

Figure 4.2: The layer structure of a strain balanced $In_{0.64}Ga_{0.36}As$ QW. $In_{0.45}Al_{0.55}As$ barrier in the structure is under tensile strain to compensate for the compressive strain in the well.

4.4 Mobility and Density results.

4.4.1. Measurement details and results summary

To determine carrier properties, Hall measurements were performed on ~8mm square pieces in magnetic fields up to 0.14T over the temperature range from 300K to 25K in a closed cycle He refrigerator. Electrical contacts are made by annealing In at 380°C-400°C in a H_2 (20%) and N_2 (80%) environment for 7-10min. Table 4.1 shows the mobility and density data obtained for the $In_{0.64}Ga_{0.36}As$/ $In_{0.45}Al_{0.55}As$ QWs along with Si δ-doping time and spacer layer thickness. The last two rows of table 4.1 summarize the maximum density and mobility obtained in a previous study.

sample	Si δ doping (sec) 2D density ($\times 10^{12}cm^{-2}$)	d (nm)	mobility (cm^2/Vs)		density ($\times 10^{12}cm^{-2}$)	
			300K	25K	300K	25K
P316	45 (1.6)	10	13,900	77,700	1.27	1.26
P317	45 (1.6)	5	13,100	66,200	1.65	1.61
P318	60 (2.2)	7.5	12,800	83, 200	2.18	2.16
P122	--	18	11,680	53,790	1.10	1.05
P123	--	10	10,800	40,830	1.25	1.20

Table 4.1: Transport properties and doping parameters of strain balanced high-density $In_{0.64}Ga_{0.36}As/ In_{0.45}Al_{0.55}As$ QWs at room and low temperatures.

These results show significant improvement on the transport properties of $In_{0.64}Ga_{0.36}As/ In_{0.45}Al_{0.55}As$ QWs, from the values of the previous experiments. The new structures were grown at conditions optimized for $In_{0.53}Ga_{0.47}As$ uniformly doped epilayers and involve a lower growth temperature of 485°C.

The structure with a 10nm spacer was δ doped with a 1.6 $\times 10^{12}cm^{-2}$ 2D density. From the Hall measurements it is evident that the 10nm thickness of the spacer layer is not optimal for all electrons to be supplied to the well. On the other hand, a 5nm spacer results in a higher density with the tradeoff of lower mobility due to increased ionized dopant scattering. The highest mobility and density were observed for the structure with a 7.5 nm spacer layer δ-doped with a 2.2 $\times 10^{12}cm^{-2}$ 2D density. For this structure (P318), a room temperature (low temperature) mobility of 12,800cm^2/Vs (83,200cm^2/Vs) and electron density of $2.18\times 10^{12}cm^{-2}$ ($2.16\times 10^{12}cm^{-2}$) was observed. The temperature dependence of the electron density and mobility of P318 is shown in figure 4.3.

A set of low-density $In_{0.64}Ga_{0.36}As/ In_{0.45}Al_{0.55}As$ QWs were also grown by lowering the doping time to lower the carrier density and varying the spacer thickness to

minimize scattering due to ionized dopants and achieve a moderate mobility. Results of this experiment are summarized in table 4.2.

sample	Si δ doping (sec)	d (nm)	mobility (cm^2/Vs)	density ($\times 10^{11} cm^{-2}$)
P322	6	7.5	44,000	7.16
P326	6	12	56,000	6.00
P323	6	15	32,000	3.30

Table 4.2: Transport properties of low-density $In_{0.64}Ga_{0.36}As$/ $In_{0.45}Al_{0.55}As$ QWs at low temperature.

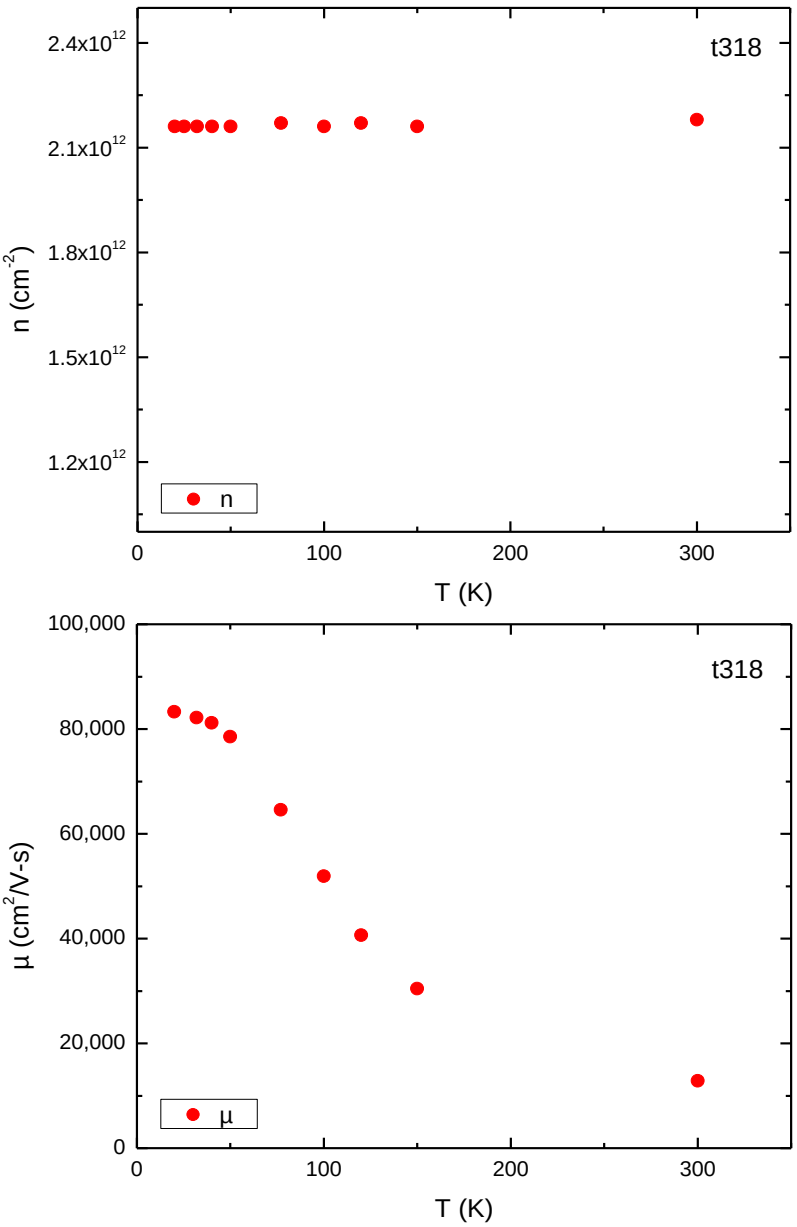

Figure 4.3: Temperature dependence of electron density and mobility of a $In_{0.64}Ga_{0.36}As$ QW.

4.4.2 Comparison of theoretical and experimental data

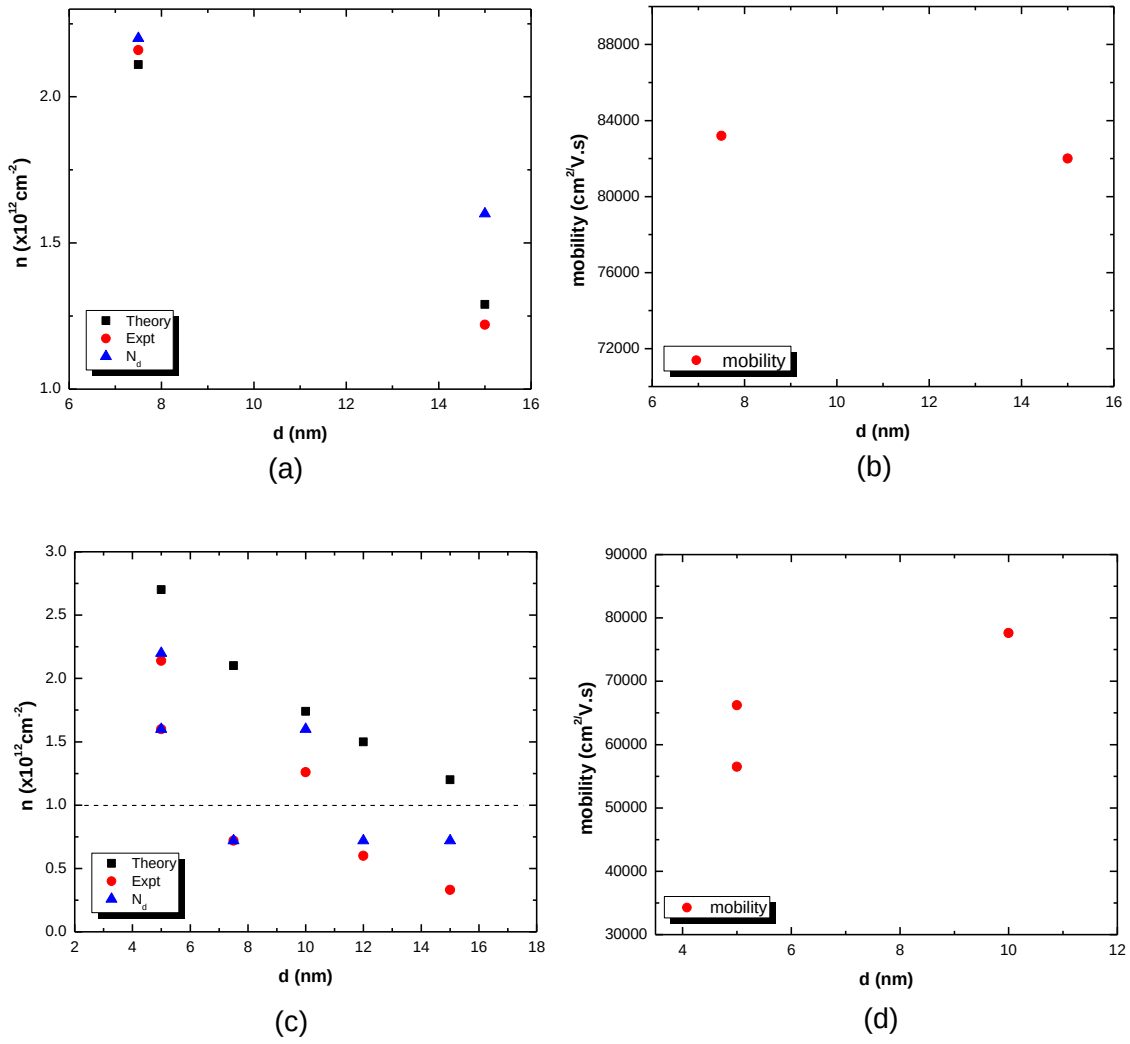

Figure 4.4: Low-temperature carrier density and mobility of QW structures in the $N_d > n_{theory}$ (a and b) and $N_d < n_{theory}$ (c and d) doping regimes. In (c) the dashed line separates the high density and low density data.

The carrier density in the well depends on donor concentration, barrier thickness, and spacer thickness. The low temperature mobility of a QW depends on interface roughness scattering, ionized dopant scattering and a dopant density threshold for a

particular spacer thickness at which the screening effects become significant[38]. Assuming the same level of interface roughness at the well-barrier interface since the well-thickness is the same for all structures in this study, the mobility of the carriers should depend only on doping and spacer parameters. At high doping densities, screening of the scattering potential by the electrons in the quantum well can reduce ionized dopant scattering enough to have a significant effect on the mobility.

Figure 4.4 shows the experimental carrier density and mobility data of QW samples and the spacer dependent carrier densities calculated using the model described in section 4.2. Theoretical and experimental densities in the $N_d > n$ regime are in good agreement (figure 4.4a). Some error in the theoretical densities (estimated to be less than 20%) is expected due to approximated values in the calculations and any theoretical aspects not considered. A lower mobility should be expected for thinner spacer thicknesses with a higher N_d since the ionized dopants reside near the well when the δ-doped layer is placed closer to the well. However, these structures show higher mobilities in the range of 83,000cm^{-2}/V-s irrespective of the doping density (figure 4.4b). This suggests that screening of the scattering potential is important in the highly doped structure at this concentration. In other words, the additional screening in the highly doped structure offsets the additional scattering expected from a reduced *d*.

Figure 4.4c shows the density data as a function of spacer for both highly doped and low doped structures, separated by the dashed line, in the $N_d < n$ regime. In structures with high doping, the carrier density is closer to the dopant density as expected except

for the structure with a 10nm spacer thickness (figure 4.4c). As the spacer thickness increases, the δ-doped layer is pushed closer to the surface. This may result in a reduction in carriers supplied to the well since carriers will begin to contribute to the surface states. Density loss in the 10nm spacer can be explained by this carrier contribution to the surface states. From available data (figure 4.4a and c), 10nm is the spacer thickness boundary at which the disagreement with the theory begins to occur in our samples. The outlier data point with the 12nm spacer thickness is not understood. The 15nm data point of figure 4.4a shows less disagreement with theory as excess carriers were provided to compensate for the loss observed in other $d \geq 10\text{nm}$ samples.

The mobilities of the structures in figure 4.4c are shown in table 4.3. These structures appear to be limited by ionized impurity scattering. The 5nm and 10nm samples have high densities. However, these densities are not high enough for strong screening effects to dominate over the scattering from closely placed ionized cores. The higher mobility is observed for the lower density sample of the two 5nm structures. The 10nm sample shows an increased mobility as the cores are farther form the well at this thickness. The 7.5nm and 12 nm low density samples show expected carrier mobilities; i.e., increasing mobility as the spacer thickness is increased. The 15nm sample does not agree with this trend. The decreased mobility of the 15nm structure may be due to a significant reduction in screening at this lowest density.

d (nm)	mobility (cm^2/V-s)	density ($\times 10^{12} cm^{-2}$)
5	56500	2.14
5	66200	1.60
10	77600	1.26
7.5	44,000	0.72
12	56,000	0.60
15	32,000	0.33

Table 4.3: Transport properties of high density and low density samples shown in figure 4.4c.

In summary, the density data show that the model is a good approximation in the $N_d > n$ regime. At low densities, $N_d \sim n$ as expected. However, experimentally this density dependence on donor concentration and spacer thickness is valid only for smaller spacer thicknesses (<10nm in our QW structures). Higher density structures have enhanced mobilities due to increased screening effects. As the density becomes lower, the mobility of carriers is limited by ionized impurity scattering.

4.5 Aharonov- Bohm Oscillations in InGaAs/InAlAs Rings

4.5.1 Aharonov- Bohm effect in mesoscopic devices

In the mesoscopic regime, the intermediate scale between microscopic and macroscopic, electrons have both wave-like and particle-like behavior. Exploring quantum interference of electrons in the mesoscopic scale has become important in quantum information processing, fabrication of mesoscopic interferometers and understanding mesoscopic physics. The Aharonov- Bohm(AB) effect, observed in mesoscopic scale structures, provides a mechanism for tuning the quantum mechanical

phase of an electron wave by means of an electric or magnetic field and controls the switching action in quantum interference devices. The simplest geometry to observe the AB effect is a ring structure shown in figure 4.5[39].

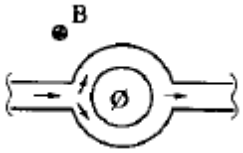

Figure 4.5: A mesoscopic ring for measuring oscillations in the resistance due to the Aharonov-Bohm effect. (T. J Thornton, *Mesoscopic Devices*, 1995)

In a mesoscopic ring, an electron wave which enters the ring from the left, splits into two partial waves and propagates along the upper and lower arms. In the ideal case the amplitudes of the two partial waves and the length they travel are the same so that in the absence of any fields they exit the ring with identical phase and interfere constructively. In the presence of a magnetic field, the phase difference between the waves when they exit the ring is $-(e/\hbar)B\pi r_i^2$ where r_i is the inter radius of the ring[40]. When the magnetic field is increased, the interference between the electron waves changes from constructive to destructive which results in an oscillation in conductance with a flux ϕ period, h/e, corresponding to a magnetic field period of $h/e\pi r_i^2$. Periodicity in the ring resistance R(B) in the presence of a perpendicular magnetic(or electric) field is known as the AB oscillations. The period in B of R(B) can be predicted from lithographic sizes using an average r in $h/e\pi r_i^2$. In experimental data, for an AB ring, the h/e oscillation period corresponding to a path length $l = \pi r$ is the strongest component in the frequency spectrum of R(B). A weaker component at $h/2e$ often exists corresponding to a path length $l = 2\pi r$. Aharonov–Bohm oscillations, quantum decoherence and amplitude modulation in mesoscopic $In_{0.64}Ga_{0.36}As/In_{0.45}Al_{0.55}As$ rings were

investigated by J. J Heremans's group at the Department of Physics, Virginia Tech[35]. Heterostructures were provided by the III-V MBE group at OU. The experimental details to observe AB oscillations, measured R(B) oscillations in low-fields, and a framework to understand the oscillation features are discussed in this section.

4.5.2 Experimental Details

The micrograph depicting an equivalent layout of AB ring used in the experiment is shown in figure 4.6. Measurements were performed on a quantum well with a width of 10nm, placed 50nm from the surface. The 2D density and mobility of the carriers are $n = 9.4 \times 10^{11} cm^{-2}$, and $\mu = 5.9 \times 10^{14} cm^2 (Vs)^{-1}$, respectively. The rings in the experiments feature an average radius of $650nm$, arm width w of $300nm$. The central antidot has radius w of $500nm$. The expected AB oscillation period is calculated to be 31 G from the average radius of the ring. AC excitation current was applied through the ring and the voltage across the AB ring was detected under a variable magnetic field B applied normal to the heterostructure area. Two identically processed samples were studied with different cool downs with T from 0.390 to 3.00 K.

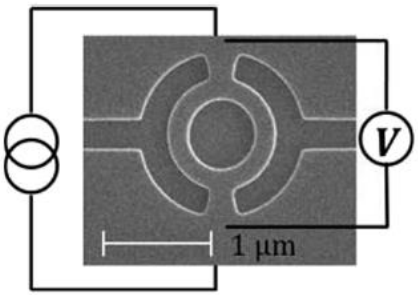

Figure 4.6: SEM micrograph of a representative Aharonov–Bohm ring, and a schematic of the four-terminal measurement setup. The darker gray areas (outlined by white borders) are etched trenches with no electrons, which act function as barriers that force the electrons to travel in the lighter gray ring-shaped areas. The rings in the experiments feature an average radius r= 650 nm, arm width w=300 nm. (S. L. Ren et al., *Condensed Matter **25** (435301)*, 2013).

4.5.3 Results and discussion

Measurements of ring resistance R(B) versus B field shows two types of periodicity-AB oscillations with a smaller periodicity and oscillation of the AB amplitude with a larger periodicity modulated with B. Pronounced AB oscillations can be clearly seen in low-B measurements performed below 0.06T(figure 4.7). The R-(B) oscillation amplitude modulated with B is apparent in the measurements over a larger range of B (figure 4.8). The Fourier transform of the low-field oscillations (figure 4.8c) displays a strong peak at ~400 -1/T which corresponds to the h/e component of the oscillations. This frequency corresponds to a period of 25G for the h/e component.

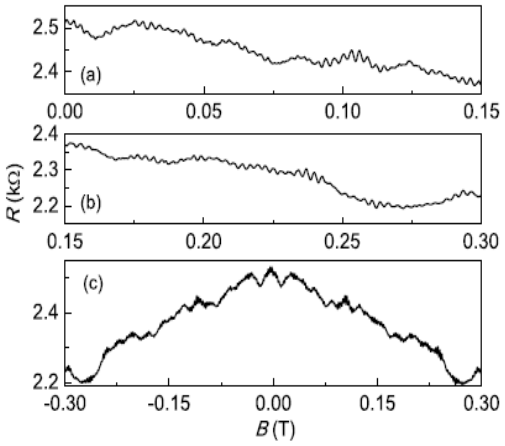

Figure 4.7: AB oscillations are seen in the measured ring resistance R(B) versus B. Panel a and b show R(B) over smaller ranges of B. In panel c, measurements over a larger range emphasize a view of the modulation with B. (S. L. Ren et al., *Condensed Matter* ***25*** *(435301)*, 2013).

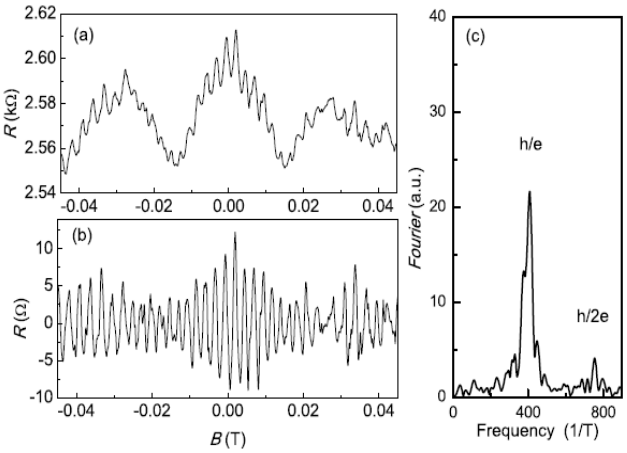

Figure 4.8: Measurements of AB oscillations in low B fields. Oscillations are measured around B= 0 at 0.4 K. The raw data is shown in panel a. The data after background removal is shown in panel (b). Panel (c) shows the Fourier transform of the data in panel (b), where h/e and h/2e modes are indicated. (S. L. Ren et al., *Condensed Matter* ***25*** *(435301)*, 2013).

For a path following the average radius of 650nm, a period of 31G is expected for the h/e component. The observed value corresponds to a preferred path having an average radius of 730nm. The difference in values arises from the finite width of the arms (lithographically w=500nm, while the conducting width is narrower due to the existence of depletion layer). This can lead to more than one preferred trajectory, deviating from the geometric centers, through the interferometer arms. Careful analysis shows that the h/e Fourier component has a central peak at 408 1/T and minor satellite peaks at 376 and 447 1/T. Using these frequencies and corresponding intensities a simplified three component model is simulated as shown in figure 4.9. A comparison of figure 4.8b and figure 4.9 shows that the local minima and maxima of the two curves' envelopes almost coincide. The approximate radii corresponding to 408 1/T; 376 1/T and 447 1/T are 734 nm, 704 nm and 768 nm, respectively, which all lie within the ring design. Therefore, the amplitude modulation of AB oscillations and the average path with radius of 730nm can be explained by the finite, electrically conducting width of the arms.

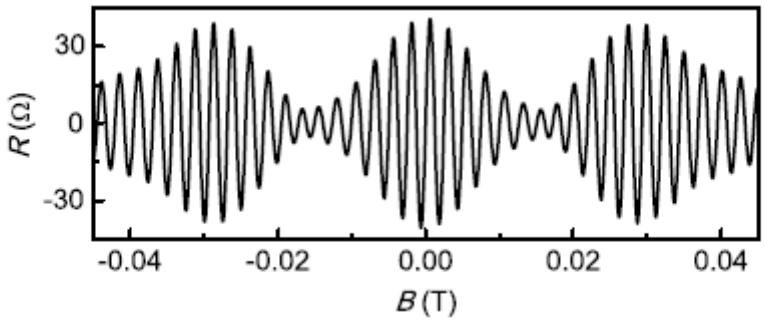

Figure 4.9: Amplitude modulation of AB oscillations modeled by the three discrete frequencies deduced from the Fourier transform in figure 4.8c: 376 1/T, 408 1/T; 447 1/T, with intensities 13.2 Ω; 21.6 Ω; 5.89 Ω respectively. (S. L. Ren et al., *Condensed Matter* ***25*** *(435301)*, 2013).

Chapter 5: Growth and Characterization of $InAs/AlAs_xSb_{1-x}$ Superlattices

5.1 Introduction

Photovoltaic (PV) devices convert incident photon energy directly into electricity. PV-technology was initially implemented in space applications[41] which required a light weight, reliable and sustainable electrical energy source to power on-board electronics. Motivated by the need for more space power, and also by growing terrestrial energy needs, researchers have steadily improved the performance of PV-cells, from an initial power conversion efficiency (PCE) yield of only ~ 25 %, over the years. However, high manufacturing costs of PV-cells and their low performance efficiencies still remain as substantial obstacles in effectively utilizing the full solar energy.

Solar cells are classified into three generations depending on their emergence. Continuous research is being conducted on each of the three generations. The first generation of cells are made of Si, a semiconductor that absorbs photons of energy equal or higher than the bandgap. However, these conventional cells, which constitute > 85% of total cell production, are slowly approaching the Shockley theoretical maximum PCE of 31%. Fundamental limitations of the first generation solar cell technology are a failure to capture low energy photons (less than the bandgap) and a loss of excess energy of an absorbed high-energy photon (much greater than the bandgap) through phonon emission. These limitations have motivated a fundamental redesign of solar technology which aims to utilize the full solar spectrum. Next generation cells involve

concepts such as multijunction devices, multi-exciton-generation (or carrier multiplication) and hot-carrier cells. The state of the art multi-junction device (MJ), referred to as the next generation cell, is basically a stack of cells with different bandgaps each capturing a different portion of the spectrum. MJ cells, which are already a well-developed technology at laboratory the level, have shown ~44% PCE[42]. Multi-exciton-generation (MEG) and hot carrier cells, which are third generation concepts, show a theoretical potential for a PCE greater than 44%[43] and 65%[44], respectively. However, they are still in the early stages of development.

This chapter starts with a review of basic solar cell electrical characteristics before discussing the molecular beam epitaxy and characterization (structural and optical) of InAs/AlAsSb superlattice (SL) structures designed to encourage the carrier multiplication processes.

5.2 Solar Cell Electrical Characteristics

This section covers basic electrical characteristics common to all solar cells. The simplest solar cell consists of a p-n diode formed by diffusion or epitaxy. Under illumination, electron-hole pairs are created in the depletion region (or within a diffusion length of it). The photogenerated electrons and holes in the depletion region are subsequently swept by the electric field to the n- and p- sides of the junction, respectively. As a result, electrical power develops across the junction which can be delivered to an external load. Figure 5.1 shows the J-V characteristics and power density of a solar cell in the fourth quadrant[45]. When measured in the dark, the current-density vs. voltage (J-V) characteristics of an efficient solar cell resembles the

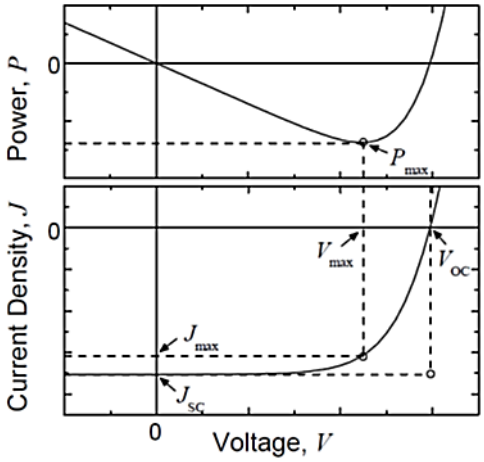

Figure 5.1 Graphs of power and current density as a function of voltage, along with key parameters, for an ideal solar cell under illumination. (R. F Pierret, *Semiconductor Device Fundamentals*, Addison-Wesley, 1996)

exponential response of the junction diode, with high current in forward bias and small current in reverse bias. Illumination generates a photocurrent in the cell in addition to the diode behavior. Under illumination, the J-V characteristics ideally represent the superposition of the dark characteristic and the photocurrent. The curve passing through the fourth quadrant indicates negative power density and hence power generation.

The J-V characteristics of an ideal device can be described by the Shockley equation with an additional photocurrent term,

$$J = J_o \left[e^{\frac{eV}{nkT}} - 1 \right] - J_{ph}$$

where J is the current density, V is the applied voltage, J_o is the reverse saturation current density of the diode, e is the elementary charge, n is the ideality factor, k is the

Boltzmann constant, and T is temperature[45]. In reality, the photocurrent will have a dependence on applied voltage, and the illumination can affect the characteristics of the diode. The most discussed figure of merits that can be found from the J-V curve of a device under a known illumination are open-circuit voltage (V_{OC}), short-circuit current density (J_{SC}), fill factor (FF), and power conversion efficiency (η).

(a) Open-circuit voltage

The open-circuit voltage V_{OC} is the voltage across the solar cell when J = 0, which is the same as the device being open-circuited. Although no power is actually produced at this voltage, V_{OC} marks the boundary for voltages at which power can be produced.

(b) Short-circuit current

The short-circuit current density J_{SC} is the current density when V = 0, which is the same as the two electrodes of the cell being short-circuited together. There is no power produced at this point. But similar to V_{OC}, J_{SC} also marks the onset of power generation. In an ideal device, the J_{SC} will be the same as the photocurrent density J_{ph}. However, like in any other electronic device, power lost through the internal series resistance of the device and recombination losses can lower the J_{SC} from this ideal value.

(c) Fill-factor

While V_{OC} and J_{SC} mark the boundaries of power production in a solar cell, the maximum power density produced P_{max} occurs at the point where product of J and V is

at a maximum in absolute value. The corresponding voltage and current density at which P_{max} occurs are denoted by V_{max} and J_{max} respectively. $|J_{max}|$ and V_{max} are always less than J_{SC} and V_{OC} because of internal resistance and recombination losses. The fill factor FF describes the power extraction efficiency of the device and is defined as:

$$FF = \frac{J_{max}V_{max}}{J_{SC}V_{OC}}$$

FF is an indication of how close J_{max} and V_{max} come to the boundaries of power production. Since a higher FF is related to a higher maximum power, a high FF is desired; however, FF is always less than one due to recombination losses and series resistance. Devices with high $|J_{SC}|$ and V_{OC} but a low FF require improvement in device quality.

(d) Power conversion efficiency

The most discussed performance parameter of a solar cell is the power conversion efficiency η and is defined as the percentage of incident irradiance I_L (power per unit area) that is converted into output power. The operating point of a cell on the J-V curve changes depending on the load. Therefore, the output power depends on the load. For consistency, the maximum output power is used for calculating efficiency. Power conversion efficiency (PCE) of a cell is defined as:

$$\eta = \frac{|J_{max}| \times V_{max}}{I_L} \times 100\% = \frac{FF \times |J_{sc}| \times V_{OC}}{I_L} \times 100\%$$

Although a higher η is often desirable, there are tradeoffs between η and cost for each solar cell technology that must be balanced. To draw comparisons between various solar cells, a standard spectrum must be chosen for the calculation of η. The AM1.5 G

spectrum in figure 5.2 is the most commonly used standard spectrum for measuring and comparing the performance of photovoltaics that are intended for outdoor use. In laboratories, power conversion efficiency measurements are often corrected based on the external quantum efficiency.

(e) External quantum efficiency

The external quantum efficiency (EQE) of a device is the fraction of incident photons of a particular wavelength that are converted into current. The short-circuit current density expected under a light source can be estimated from the EQE and the spectral irradiance of the light source by integrating the product of the EQE and the photon flux density. For the standard AM1.5 G spectrum (figure 5.2)[45], the calculation is

$$J_{SC} = \int_0^{\infty} eEQE(\lambda)\frac{\lambda}{hc}E_{\lambda}^{AM1.5G}(\lambda)d\lambda$$

where $E_{\lambda}^{AM1.5G}$ is the spectral irradiance of the AM1.5 G spectrum, λ is the wavelength, h is Planck's constant, c is the speed of light, and e is the elementary charge.

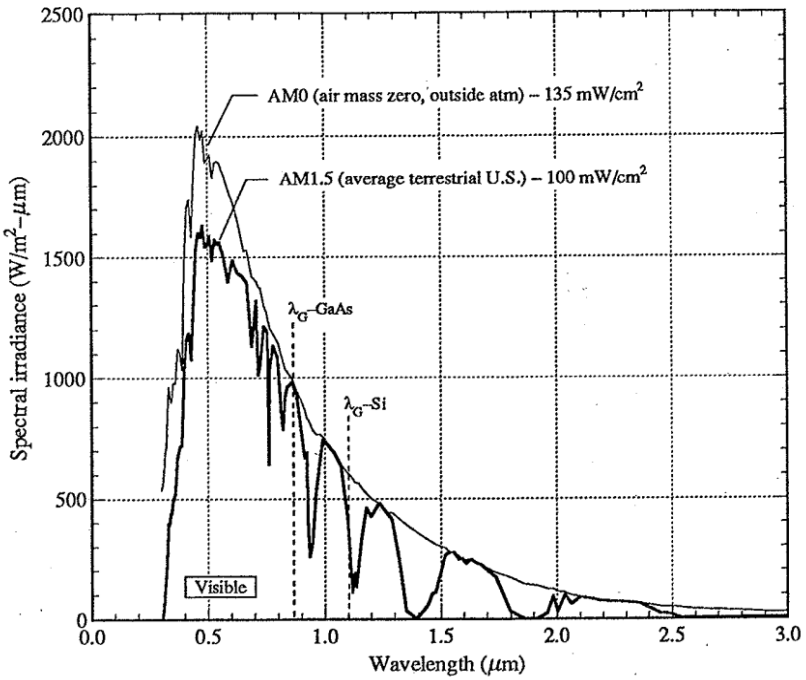

Figure 5.2: Solar spectral irradiance. (R. F Pierret, *Semiconductor Device Fundamentals*, Addison-Wesley, 1996)

5.3 Principles and Literature Overview: MEG/CM and Hot Carrier Cells

Two fundamental ways to enhance power production in a solar cell are an increment in current or voltage generation or a combination of both. The MEG, also known as the carrier multiplication (CM) process, is a means to generate more current. The HC design concentrates on fast extraction of hot carriers to achieve higher current and voltage.

The MEG concept proposes utilizing high energy carriers to excite additional electrons per absorbed phonon to the conduction band, which would increase the photocurrent of the cell (figure 5.3). Schaller and Klimov presented the first report on MEG observation in PbSe nanocrystals[46]. They reported that the excitation energy threshold for the efficient formation of two excitons per photon is ~$3E_g$. Subsequent work also reported efficient MEG in several quantum dot (QD) systems[47,48] and in bulk systems[49]. For InP QDs, an MEG threshold of $2.1E_g$ was reported[50]. Theoretical predictions state that carrier multiplication effects in 0.7 eV to 0.8 eV bandgap systems can lead to a PCE >44%[43].

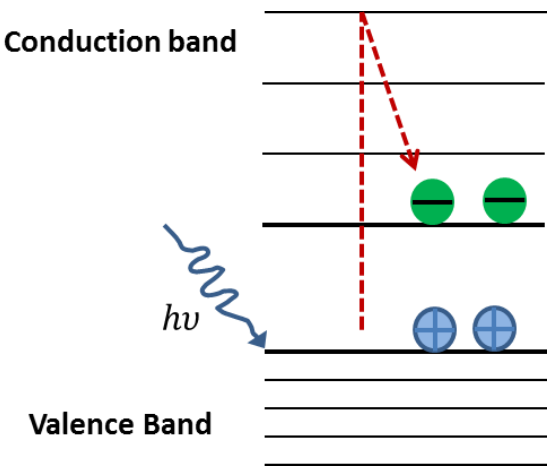

Figure 5.3: Schematic of a single hot electron generating bi-excitons. In a MEG process, after absorption of a photon, carriers have sufficient energy to promote another electron across the bandgap, yielding more than one carrier pair per absorbed photon. Compared to energy levels of bulk systems, the larger separation of energy levels in confined systems inhibits phonon cooling. This enhances the MEG process and reduces energy wasted as heat.

The HC design attempts to minimize thermal losses by extracting carriers at elevated energies within a narrow range. A schematic of a HC cell with energy selective contacts (ESCs) shown in figure 5.4[51]. The HC-SC was originally proposed by Ross and Nozik[52]. Carrier cooling in bulk semiconductors occurs within 10–100 ps[51], therefore this cell requires substantial delay in carrier cooling in the hot carrier absorber.

Hence, the key requirements of a HC photovoltaic device would be an absorber which can significantly reduce thermalisation of photoexcited hot carriers, that allow carriers within a narrow energy range to pass through to the metal contacts, and successful integration of these without any performance loss of either. The suitability of resonant tunneling structures based on quantum wells [53]and dots[54] has been investigated for the role of ESCs. The discrete DOS of QDs limits the absorption energy range. The continuous DOS of MQW and SL structures allow photon absorption across a wide range. Evidence suggests that hot-photocurrents can be extracted from very thin absorber layers[53] . The theoretical efficiency of a HC solar cell is calculated to be as high as 65% for one sun and 85% for maximum concentration[44], for a single bandgap semiconductor.

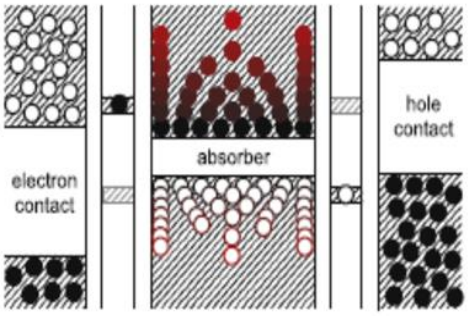

Figure 5.4: Schematic of a hot carrier solar cell. Hot carriers in a small energy range are extracted through an energy selective contact into a macroscopic contact. (D. König et al., *Physica E: Low-dimensional Systems and Nanostructures* **42** (10), 2862-2866, 2010).

5.4 Key Features of the InAs/$AlAs_xSb_{1-x}$ Superlattice Design

We grew a series of InAs/$AlAs_xSb_{1-x}$ superlattice (SL) structures designed to observe MEG/ CM effects in InAs quantum wells. The key features are a SL bandgap tuned to E_g~0.8 eV by quantum confinement and large-gap $AlAs_xSb_{1-x}$ barriers that provide a well height greater than $3E_g$, to encourage high energy carrier excitation and subsequent biexciton formation in the well. $AlAs_xSb_{1-x}$ barriers have an indirect gap of ~1.6eV and a direct gap of 2.5eV. The thin barrier layers can inhibit indirect transitions (~1.6eV) and thereby promote direct transitions (2.5eV) in the barrier. The small InAs/$AlAs_xSb_{1-x}$ valence-band offset should facilitate hole transport. Figure 5.5 shows a simplified model of band alignment and energy states for a series of 2.4nm InAs QWs with 2nm and 10nm barrier thicknesses. There are three confined electron subband groups for this configuration (figure 5.5a and 5.5b). Wells with thin barriers (2nm) are strongly coupled due to large overlap of wavefunctions of individual wells. Wells with thicker barriers (10nm) have less direct interaction between them. However, some degree of coupling exists as the wavefunctions still overlap in the barrier. The lowest transition energy for these QWs is closer to 0.9eV. As the number of wells is increased, the strength of coupling between the wells introduces a quasi-degree of freedom in the z-direction, which results in continuity in E_z similar to bulk. This can be visualized as a miniband formation at the quantized state. Then the effective bandgap (separation between the electron and hole minibands) is lowered due to miniband formation(figure 5.5c and 5.5d)[55]. Therefore, the lowest transition energy can be controlled by the strength of coupling between the wells, and hence by miniband formation. The model predicts the effective bandgap of the SL system to be closer to 0.7eV (figure 5.5c and

d). Experimentally observed values of the effective bandgap will depend on the barrier composition, layer thicknesses and strain of layers. For carrier multiplication, the energy of a hot electron must be sufficiently high to produce an electron-hole pair when it relaxes to the ground-state subband ($E_{hot} - E_{edge} > E_{gap}$). Values predicted by the model suggest that relaxation from hot electrons in the third subband of the QWs can excite additional carriers across the QW bandgap.

The calculation of energy band profile, photoluminescence (PL) experiments, PL data analysis and I-V characterization of the InAs SLs were performed by Dr. I. Sellers's Photovoltaics Materials & Device Group at the Department of Physics and Astronomy, University of Oklahoma. XRD characterization of some chosen structures (figure 5.11) was performed by T. Zederbauer and G. Strasser, at the Institute of Solid State Electronics, Vienna University of Technology, Austria.

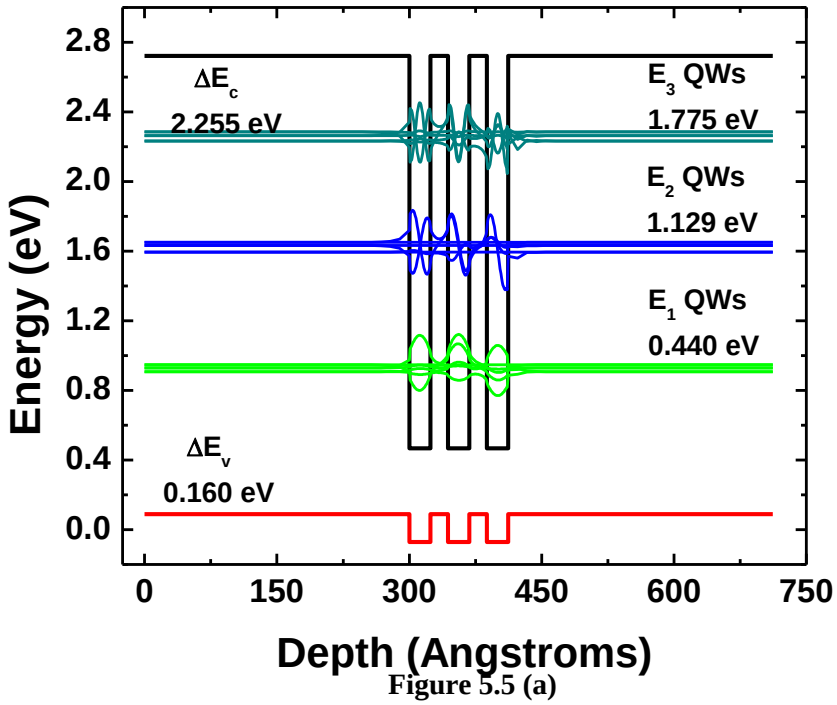

Figure 5.5 (a)

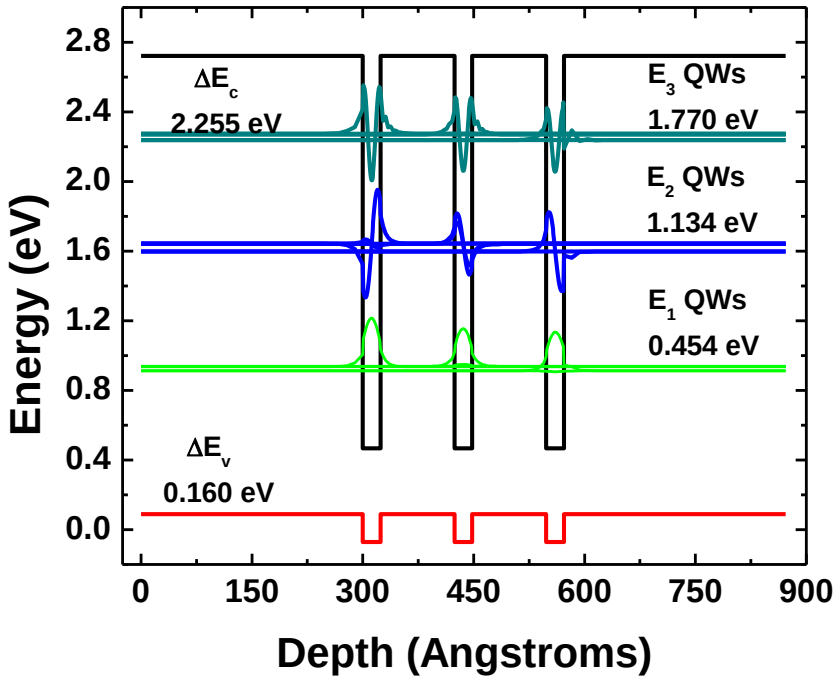

Figure 5.5 (b)

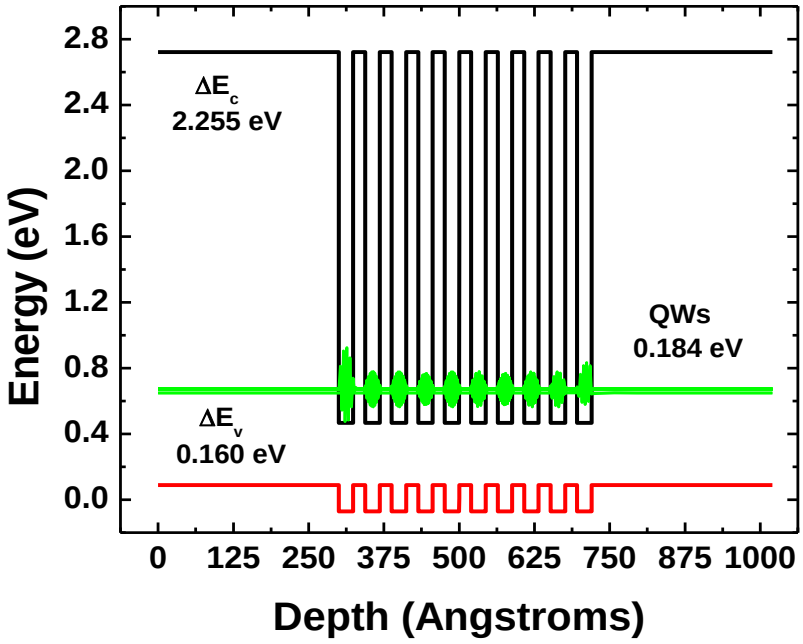

Figure 5.5(c)

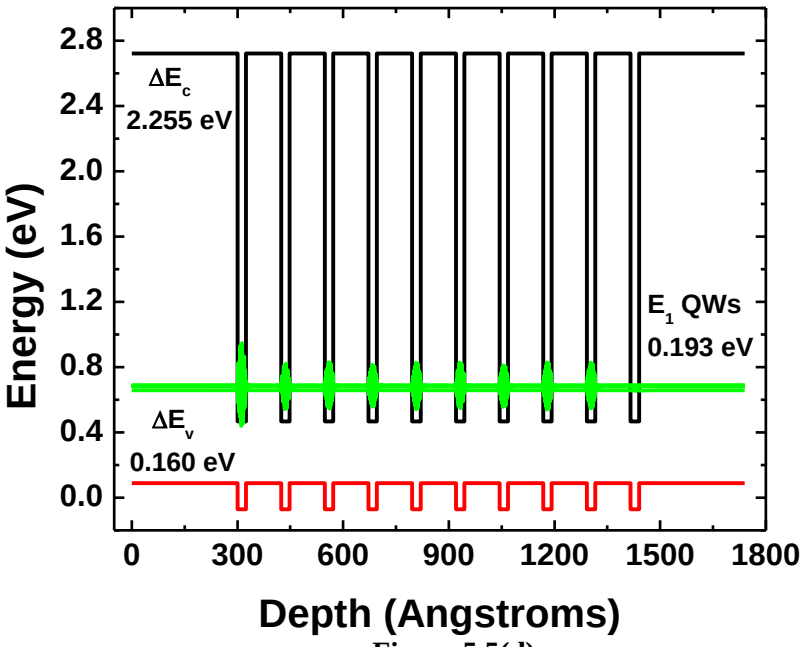

Figure 5.5(d)

Figure 5.5: Calculated energy-band profile for InAs/AlAsSb superlattices developed to investigate carrier multiplication effects. Panels (a) and (b) show energy states for a few quantum wells with barrier thicknesses 2nm and 10nm, respectively. Three subband groups are present for these wells. Bandgap of these wells falls above 0.8eV. Panels (c) and (d) show the miniband formation for these wells when the numbers of wells are increased. The effective bandgap falls below 0.8eV in the SLs. The calculated value of the effective band gap is closer to 0.7eV.

5.5 InAs/ $AlAs_xSb_{1-x}$ Superlattices Growth

5.5.1. Ternary alloy calibration

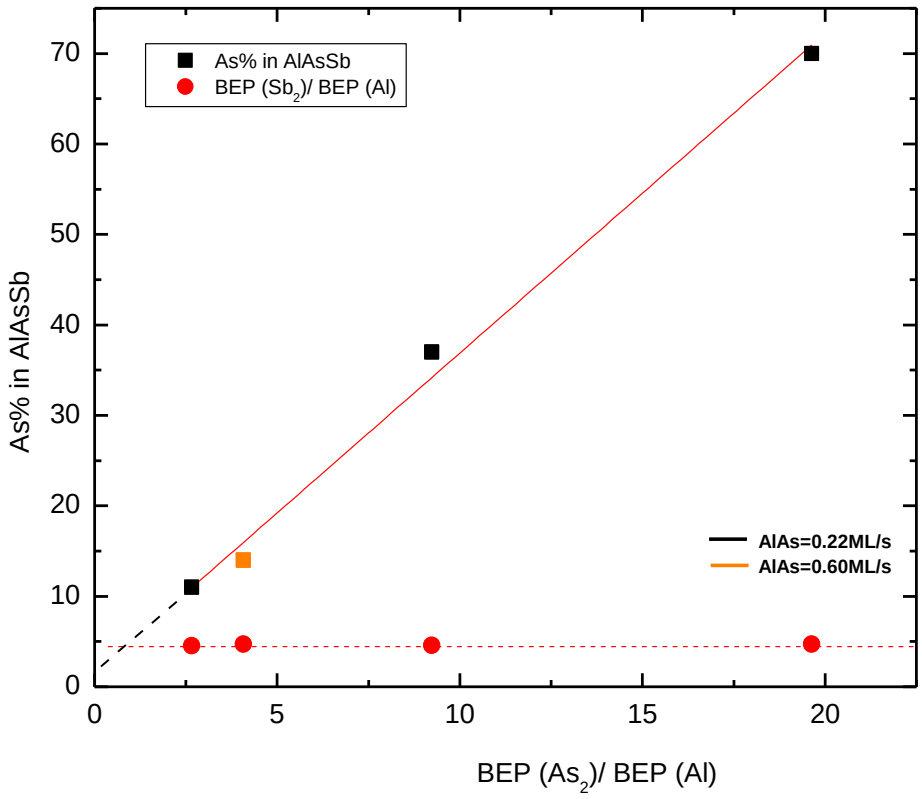

Figure 5.6: Arsenic mole fraction in AlAsSb epilayers versus BEP of As_2 normalized with BEP of Al. The linear sloped represents the regression fitting of the experimental points. Points along the horizontal dotted line correspond to the BEP (Sb_2)/BEP (Al) ratio of the layers.

Growth of mixed-group-V compounds is difficult due to the non-unity sticking coefficient of the group V species. Reproducibility then requires precise control of the As and Sb flux ratio, specifically through the control of the Arsenic flux. A series of $AlAs_xSb_{1-x}$ epitaxial layers were grown on GaAs (001) substrates to obtain growth conditions for the $AlAs_xSb_{1-x}$ alloy, lattice matched to InAs. Structures of thickness 0.5 μm were grown at a rate of 0.22 ML/s, in a range of substrate temperatures ~520-550°C. This range of growth temperature was chosen based on the typical AlSb growth

temperature used in our growths and optimized through RHEED observation. A (3×1) RHEED pattern was observed while the growth was in progress (figure 5.7). HRXRD measurements were performed on these structures to determine the composition of the alloy. A sample XRD profile of the alloy is shown in figure 2.4. The growth scheme involved fixed Al and Sb flux (or growth rate), and a varying As flux with V/III ratio higher than 1 so that the growth rate is controlled by the arrival rate of the group III species. A four times higher arsenic flux than antimony flux was initially chosen so that the arsenic fraction of the group V flux controls the composition of the alloy. These parameters resulted in a 0.7 arsenic mole fraction in the alloy.

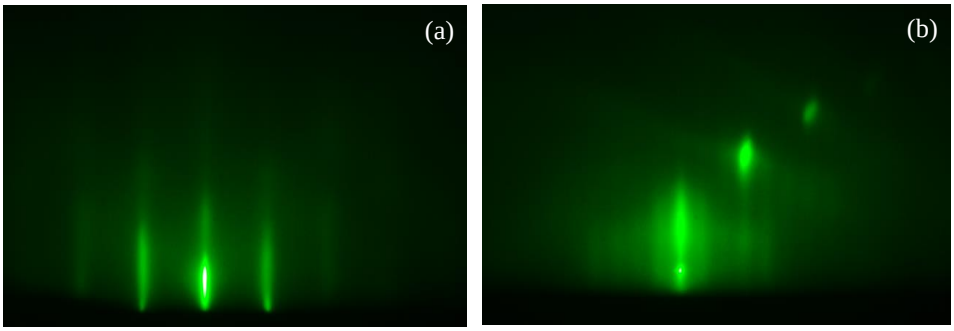

Figure 5.7: RHEED pattern of ~300nm AlAsSb on GaAs (001) substrate (a) 1x along [1 0 0] (b) 3x along[1 $\bar{1}$0].

Figure 5.6 shows XRD characterization data and associated growth conditions of $AlAs_xSb_{1-x}$ for different compositions. The data points show a linear dependence of arsenic incorporation with the normalized arsenic flux. The plot of normalized antimony flux associated with the epilayers is also shown in figure 5.6. Under constant BEP (Sb_2)/BEP (Al) growth conditions, arsenic incorporation depends only on arsenic flux even when the Sb:As ratio is close to one (table 5.1). Arsenic incorporation at a higher AlAs growth rate is very close to the best fit line indicating the linear dependence does

not change within the high V/III growth regime. Therefore this simple growth method, in which the lattice constant of the alloy is determined by BEP (As_2)/BEP (III) with Arsenic filling the group V sites first and then antimony filling the remaining sites, is useful for obtaining various compositions of the mixed group V alloy. A BEP difference of 0.2×10^{-7} torr for As introduces a 1% lattice mismatch in the alloy. The error in the two data points away from the regression line is within the limits of inaccuracy that can occur in flux readings. Therefore careful measurement of the BEP of sources is necessary to obtain a preferred composition.

For superlattice structures that required the alloy to be grown at different growth rates (for AlAsSb and GaAsSb), growth parameters (As/III & Sb/As ratios) were chosen from the calibration plot and re-characterized to make improvements based on their XRD measurements. The thin superlattice layers involve growth time in the order of seconds. Therefore the transient nature of the sources must be considered in order to ensure the growth of intended compositions. HRXRD measurements on the first superlattice structure resulted in a smaller lattice constant than the expected according to the m=0 (average lattice constant of the superlattice). This indicated less antimony incorporation than intended. Assuming the QW thickness was consistent, an ~8.6% higher antimony flux than the flux for bulk growth was found necessary to achieve the required alloy composition in the superlattice.

Sample	$\frac{BEP\ (As_2)}{BEP\ (Al)}$	$\frac{BEP\ (Sb_2)}{BEP\ (Al)}$	As% in Alloy
T611	19.6	4.72	70
T612	9.22	4.59	37
T618	4.07	4.69	14
T616	2.66	4.55	11

Table 5.1: Growth parameters of AlAsSb layers grown to calibrate alloy composition with a varying arsenic flux.

It must be noted that antimony segregation is possible in the grown epilayers and SL structures. QD systems and 2D layers with ternary alloys contain antimony have exhibited increasing segregation of Sb with increasing growth temperature[56] and concentration[57, 58, 59, 60]. AlAsSb growers have reported difficulty in growing a preferred composition and in reproduction of the alloy due to precise group V pressure requirements[61,62]. Therefore, producing high quality samples of the intended SL structure can be challenging due to high sensitivity to flux ratios, variations in the substrate temperature, and Sb segregation in the alloy.

5.5.2 Growth of superlattice structures

Prior to full solar-cell structure growth, a few optical structures were grown to determine the transition energies by PL absorption and structural quality by HRXRD measurement. These samples were grown on GaAs (001) 2° off towards <110> substrates, with an InAs buffer layer of thickness≥ 2μm. The layer structure of a typical

optical superlattice is shown in figure 5.8. An InAs buffer layer was grown at a rate of 0.66ML/s with a V/III ration of ~15and at a substrate temperature of 450°C[63]. For the superlattice layers, the growth rate of InAs was chosen as 0.1ML/s with V/III~9 and the substrate temperature as 465°C. Although the As source cell is equipped with a valve control for flux variation, residual As remains in the chamber for a long time. Therefore a common arsenic flux of 5×10^{-7} Torr for the superlattice layers was chosen to optimize conditions for the growth of the AlAsSb barrier layer. A summary of grown structures that showed PL spectral features in the energy range of interest is shown in table 5.1.

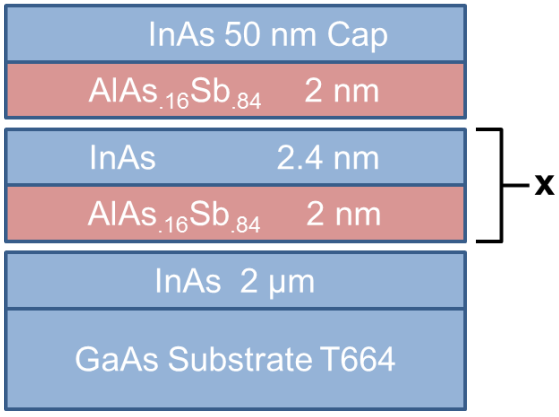

Figure 5.8: A typical InAs SL structure grown to determine the optical properties of the proposed solar cell design. The structures were grown on GaAs(001) 2° off substrates with a 2µm InAs buffer.

Sample (Barrier Thickness)	X (number of SL periods)	Al BEP (Torr)	As BEP (Torr)	Sb BEP (Torr)	(As+Sb)/As BEP ratio
T664(2nm)	80	1.24×10^{-7}	5×10^{-7}	6.10×10^{-7}	2.22
T676(2nm)	30	1.25×10^{-7}	5×10^{-7}	6.38×10^{-7}	2.28
T673(10nm)	30	1.25×10^{-7}	5×10^{-7}	6.38×10^{-7}	2.28

Table 5.2: Summary of growth parameters for optical SL structures.

5.6 Preliminary Structural Characterization

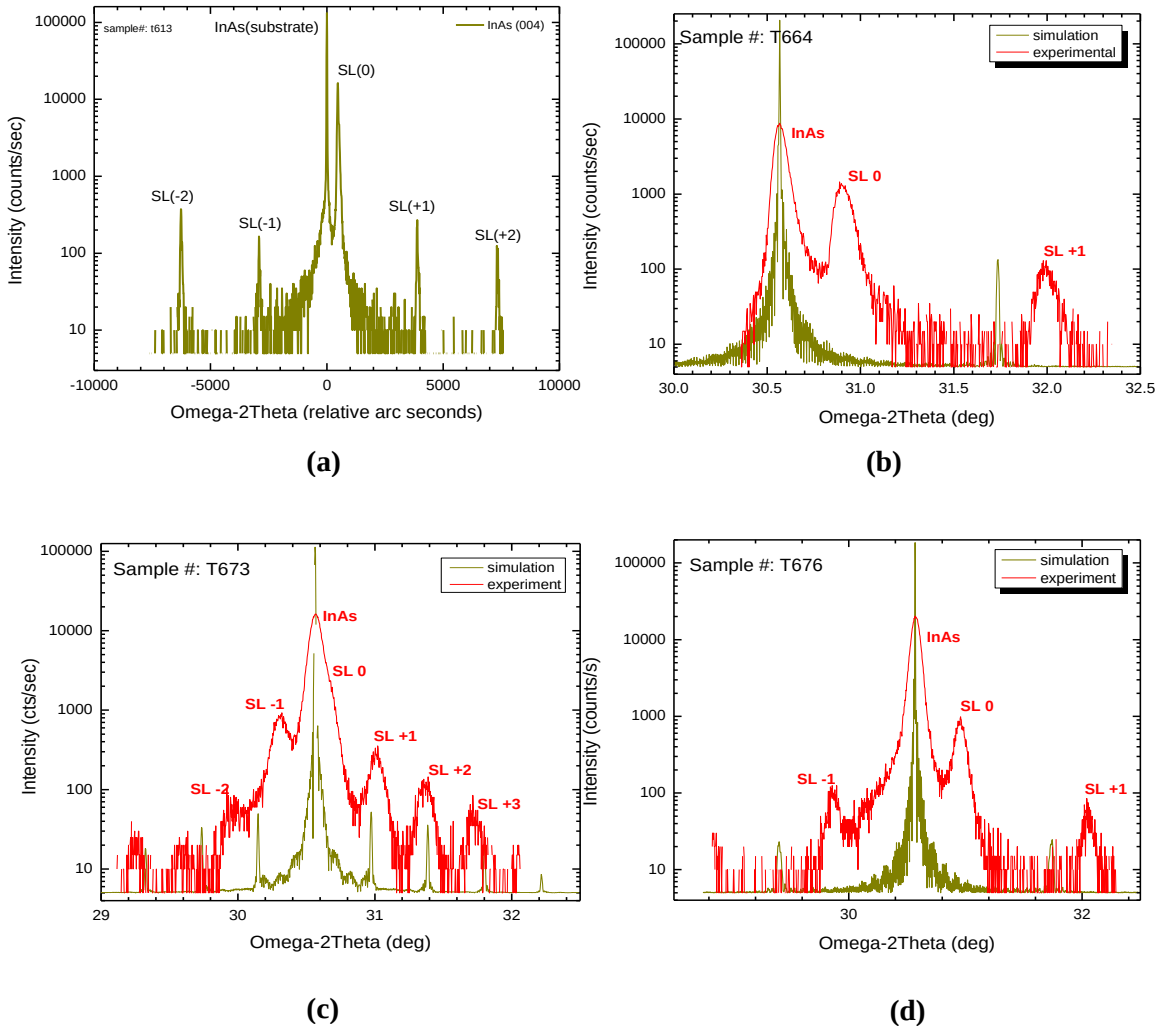

Figure 5.9: Diffraction profiles of optical InAs/ $AlAs_xSb_{1-x}$ superlattice structures grown on (a) an InAs substrate and (b, c, d) a GaAs substrate. Panels (b) and (d) are structures with 2.4nm/2nm well/barrier thicknesses. The structure for figure (c) has a 10nm barrier.

The sample position was first optimized for the GaAs (004) diffraction peak with the Ω scan mode and then scans were performed with the Ω-2θ mode to observe reflections from InAs (004) planes. Scans were centered on the InAs (004) peak to obtain maximum intensity from superlattice peaks. Figure 5.9a shows the experimental XRD

intensity profile of a structure grown on an InAs substrate with well and barrier thicknesses of 2.8nm and 2nm, respectively. Sharp peaks for this sample indicate coherence of the interfaces and that good growth quality of the designed structure can be achieved in lattice matched conditions. Figure 5.9b, c and d are the diffraction profiles of structures grown on GaAs substrates. Peaks of these structures appear broader compared to simulated peaks as a result of imperfect periodicity in the structure, which is typical in lattice mismatched growths. Samples T673 (figure 5.9c) and T676 (figure 5.9d), which have different barrier thicknesses, were grown under similar conditions. However, the 0^{th} order peaks of these structures have different offsets from the InAs (004) peak, indicating different out-of-plane lattice constants of the superlattice unit, originating from difference in strain or stoichiometry as the layer parameters change. The thickness of the superlattice unit is calculated to be 4.7nm in samples T664 and T676 (equation 2.22). The SL unit thickness and the closely spaced average lattice constant peak show a good match to the designed parameters.

5.7 Optical Characterization

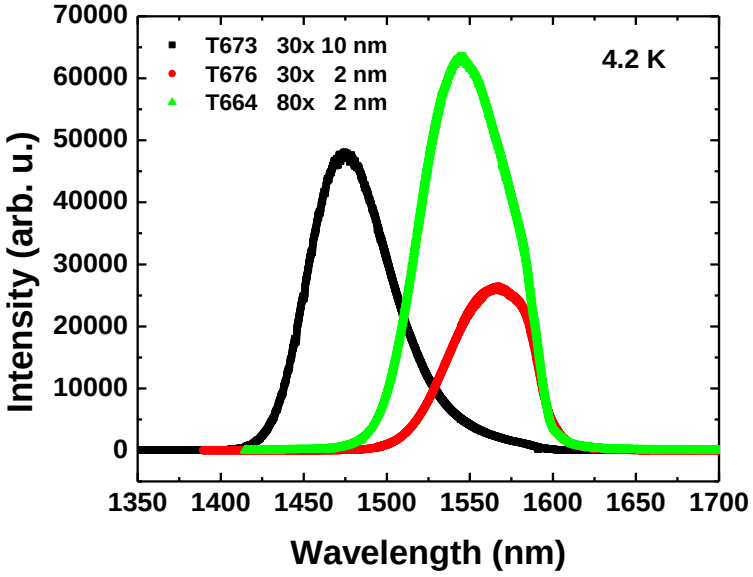

(a)

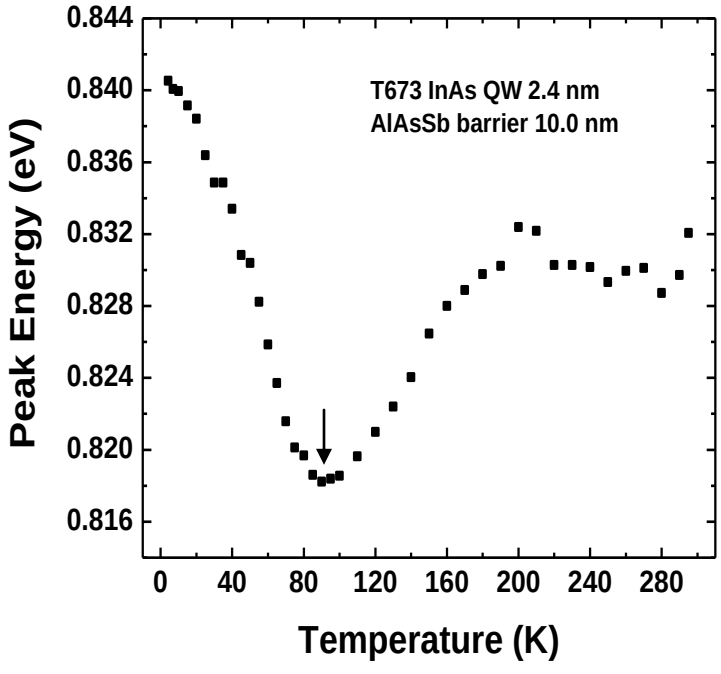

(b)

Figure 5.10: (a) Photoluminescence spectra at 4.2K from three InAs/AlAsSb superlattice structures. (b) Peak energy dependence on temperature.

The optical SL structures were characterized with photoluminescence spectroscopy to determine the transition energy levels of the structures. PL spectra of the SL wells with 2nm and 10nm barriers at low temperature is shown in figure 5.10[55]. Samples T664 (80cycles) and T676 (30cycles) have the same layer structure with a 2nm barrier. Peaks from these samples appear aligned at an energy value of 0.80eV (1550nm). Sample T673, which has a similar layer structure with 10nm barrier thickness, shows a blue shifted peak at 0.85eV (~1475nm in wavelength). As discussed in section 5.4, when the barrier thickness is increased the degree of freedom in the z-direction is lessened and the transition energy becomes higher than that of a coupled SL system. Therefore these observations agree with the expected dependence. Figure 5.10b shows the peak energy variation with temperature for one of the SLs. The observed localization of energy, ~ 10meV from 80K-90K, is typical in narrow wells due to alloy fluctuations.

5.8 Investigation of an Additional Absorption Layer

A $GaAs_{0.09}Sb_{0.91}$ layer, lattice matched to InAs, has an energy gap of ~0.7eV. This layer can capture additional high energy photons that escape absorption in the well region and create more e-h pairs. A second series of structures were grown with a 4μm InAs buffer layer on a GaAs substrate with a $GaAs_xSb_{1-x}$ layer and characterized with diffraction[64] and optical methods.

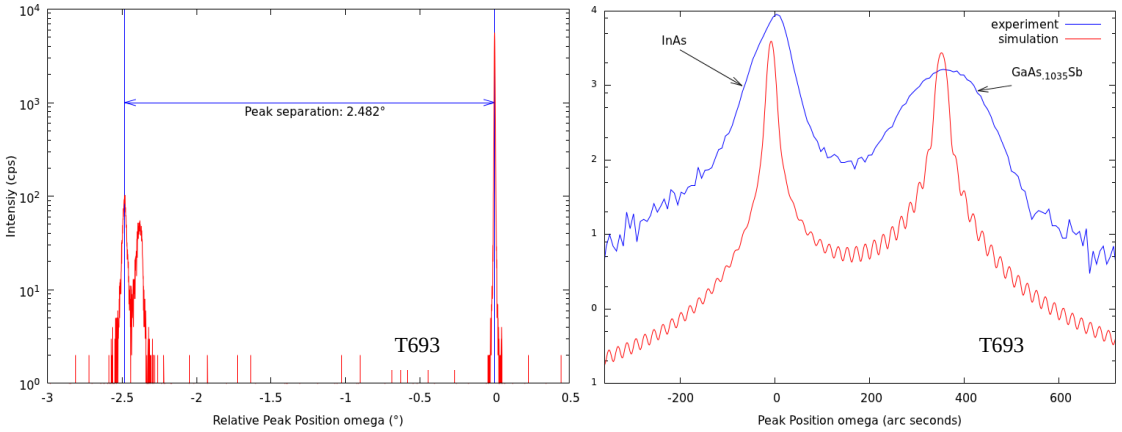

(a) (b)

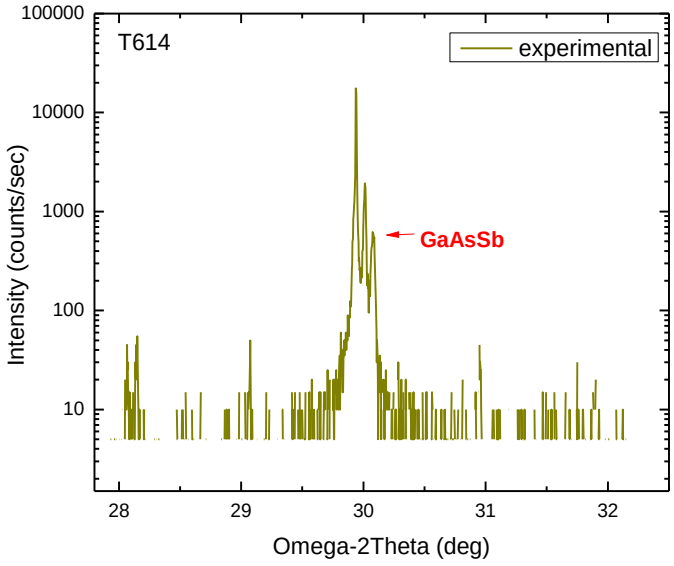

(c)

Figure 5.11: HRXRD scans of structures T693 (a and b) T614 (c) with the GaAsSb layer. In panel (a), the 4µm InAs layer in T693 shows full relaxation. In panels (b) and (c) the mole fraction of As in the GaAsSb layer is 0.10 (b and c), which is closer to the desired value of 0.09.

Initial XRD characterization of the $GaAs_xSb_{1-x}$ layer was performed on an optical structure (T614) and the As mole fraction in the alloy was calculated as ~ 0.10 (figure

5.11c). The HRXRD measurement of a more recent solar cell structure (T693) is shown in figure 5.11a and b. In this structure, the InAs (004) and GaAs (004) peak separation is 2.482°. This is very close to the theoretical separation of 2.465°. Therefore the buffer layer can be assumed to be fully relaxed. Due to the high lattice mismatch with the substrate, a broadened $GaAs_xSb_{1-x}$ peak is observed. From the position of the $GaAs_xSb_{1-x}$ peak position, the As mole fraction was found to be 0.1035. This value is very close to the desired mole fraction 0.09. PL measurement on a structure with a $GaAs_xSb_{1-x}$ layer (figure 5.13) showed only a very weak signal. Therefore, at this stage, it is inconclusive whether $GaAs_xSb_{1-x}$ can contribute as an efficient absorber.

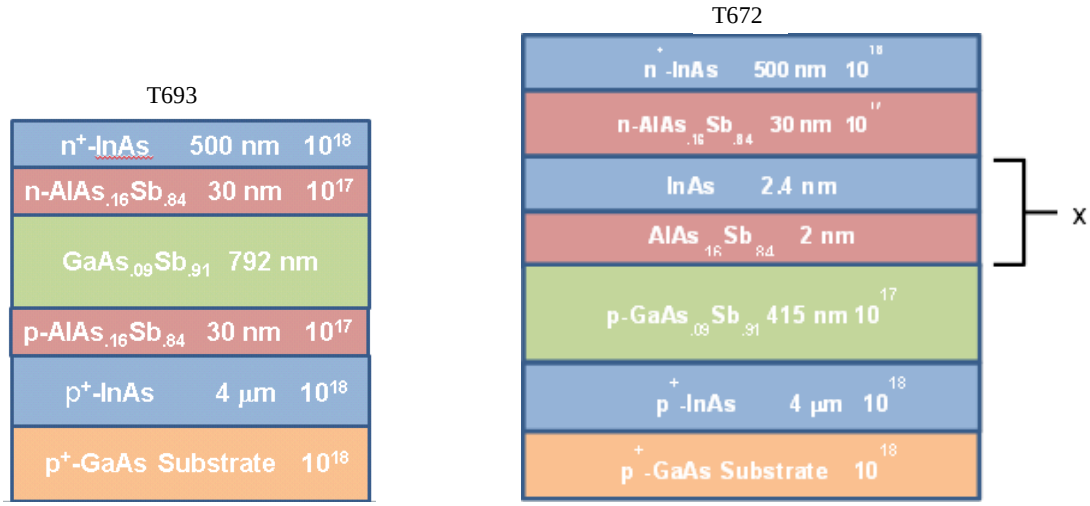

Figure 5.12: Optical structures with $GaAs_xSb_{1-x}$ layers. (a) Structural characterization was performed on sample T693 to determine the group V mole fractions in $GaAs_xSb_{1-x}$. (b) Sample T672 was optically pumped to observe features that may correspond to the $GaAs_xSb_{1-x}$ layer.

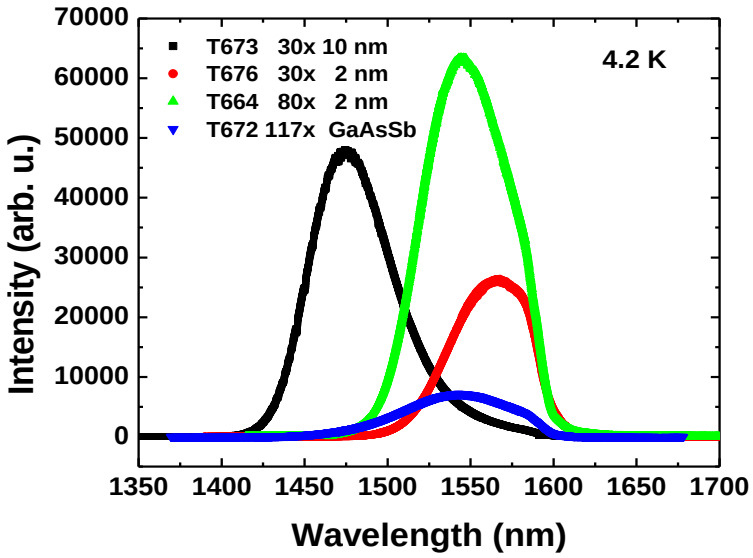

Figure 5.13: PL spectrum of T672, which contains a SL and a GaAsSb absorption.

5.9 Summary

In superlattices, the effective bandgap of a QW can be tuned by confinement and miniband formation. An InAs/AlAsSb SL structure was designed to study hot carrier and CM effects. It had a bandgap tuned to E_g~0.8 eV and a barrier tall enough for the subband energy spacing to be larger than the bandgap. Initial SL structures designed to determine structural and optical properties of the SLs were presented in this chapter. A modeled structure with 2nm/2.4nm well/barrier thicknesses shows an effective bandgap of ~0.7eV for the SLs. Optical characterization of these structures show good agreement with the model prediction with a PL peak observed at ~0.8eV. Preliminary level structural analysis shows SL features close to the simulated peaks and a SL unit thickness of 2.7nm. A method to obtain a specific AlAsSb alloy composition was also described.

5.10 Additional Details and Suggestion for Further Work

5.10.1 Fitting of recombination processes in the QWs

A higher rate of radiative recombination will indicate a suitable quality of the structure as a solar cell material. The relative importance of Shockley-Read-Hall, Auger and radiative recombination mechanisms can be deduced by analyzing the PL intensity as a function of laser power input, because each mechanism has a different power dependence. Figure 5.13 shows the results of PL data analysis for an InAs SL structure. The analysis indicates that Shockley-Read-Hall recombination (a two-step recombination process in which conduction electrons relax to the defect level and then relax to the valence band annihilating a hole) dominates at room temperature[55,65]. It will be useful to study how the recombination processes are different in a lattice matched structure grown on an InAs substrate.

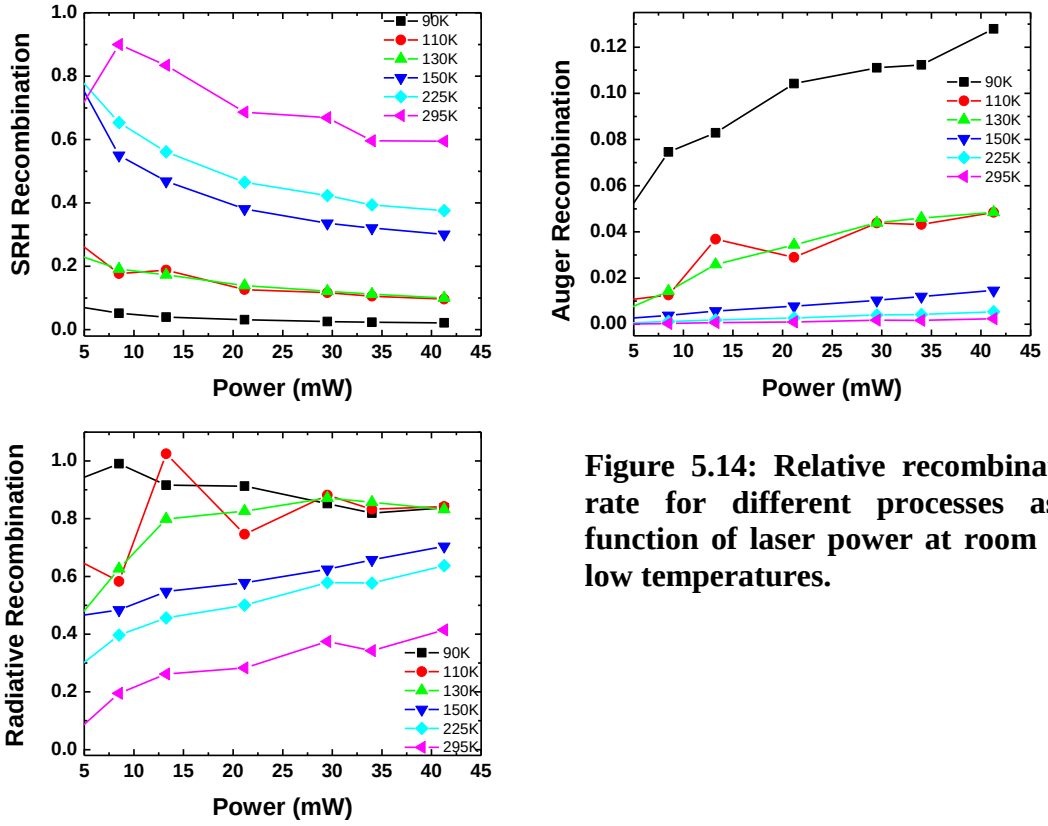

Figure 5.14: Relative recombination rate for different processes as a function of laser power at room and low temperatures.

5.10.2 Probing hot-carriers via luminescence

The luminescence at energies greater than the bandgap (~0.85eV) energy arises the from the hot-carrier population. Figure 5.15 shows the PL intensity-energy spectrum for the excitation wavelength $\lambda = 442nm$ at 90K.

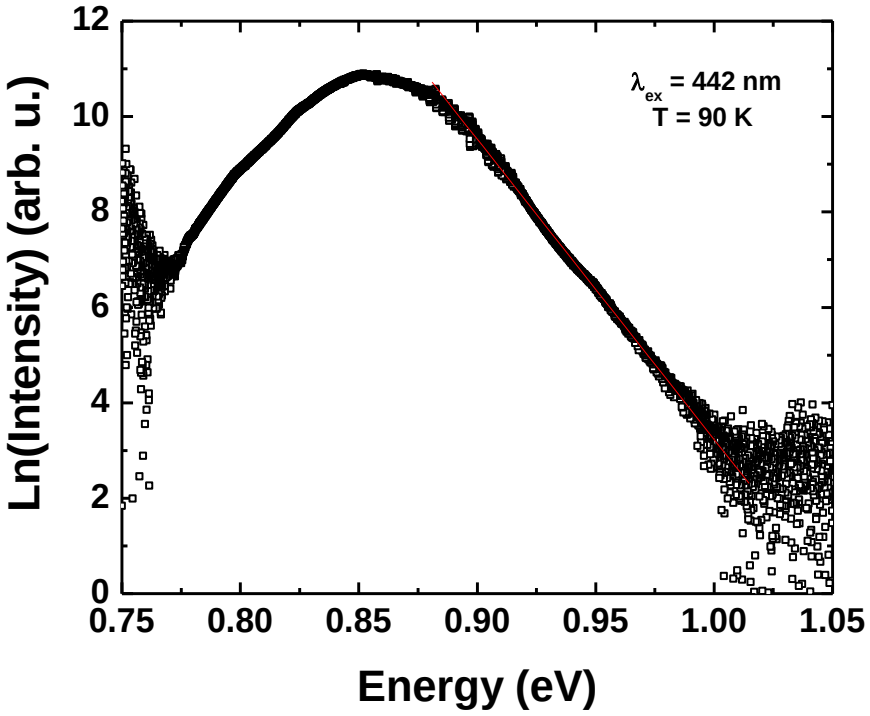

Figure 5.15: PL intensity-energy spectrum for a 442nm excitation wavelength at 90K.

The temperature of the hot-carriers can be extracted from the intensity-energy spectrum by performing a Maxwellian fit at the high energy tail described by:

$$I_{PL}(h\upsilon) \propto e^{-\frac{h\upsilon}{k_B T_H}}$$

where I_{PL} is the PL intensity, $h\upsilon$ is the photon energy, k_B is the Boltzmann constant, and T_H is the hot carrier temperature[66]. A shallower high energy slope corresponds to larger

temperature difference $\Delta T = T_H - T$, where T is the measurement temperature. A larger ΔT can be expected as the excitation power is increased as more hot carriers will be generated. A smaller ΔT can be expected as the temperature is increased because more phonons become available. Figures 5.16a and 5.16b show ΔT for different excitation powers measured at temperatures 4K to 295K, respectively. At low temperatures from 4K to 90K, ΔT decreases with T and increases with P as expected. For temperatures higher than 90K, the carriers stay hot at all temperatures (i.e. ΔT does not decrease with T). The temperatures difference is independent of P above 150K (i.e. ΔT does not increase with P). At temperatures higher than 90K, the valence band offset may be negligible compared to the thermal energy and holes may no longer be localized for recombination. The availability of only a few holes for recombination may be the reason for carriers remaining hot at these temperatures. Although hot-carrier effects can be probed via luminescence, observing a signature of CM in a continuous PL spectrum may not be possible if the biexciton decay time is very short. MEG generation in nanocrystals and QDs are shown to occur in less than 200fs using ultrafast transient spectroscopy with sub-fs pulses[43,46]. Around 300ps, which is the typical time resolution in PL spectroscopy, the additional exciton is lost and only evidence of a single exciton is reported. Therefore, it might not be possible to observe CM effects directly in the SL system using continuous PL spectroscopy.

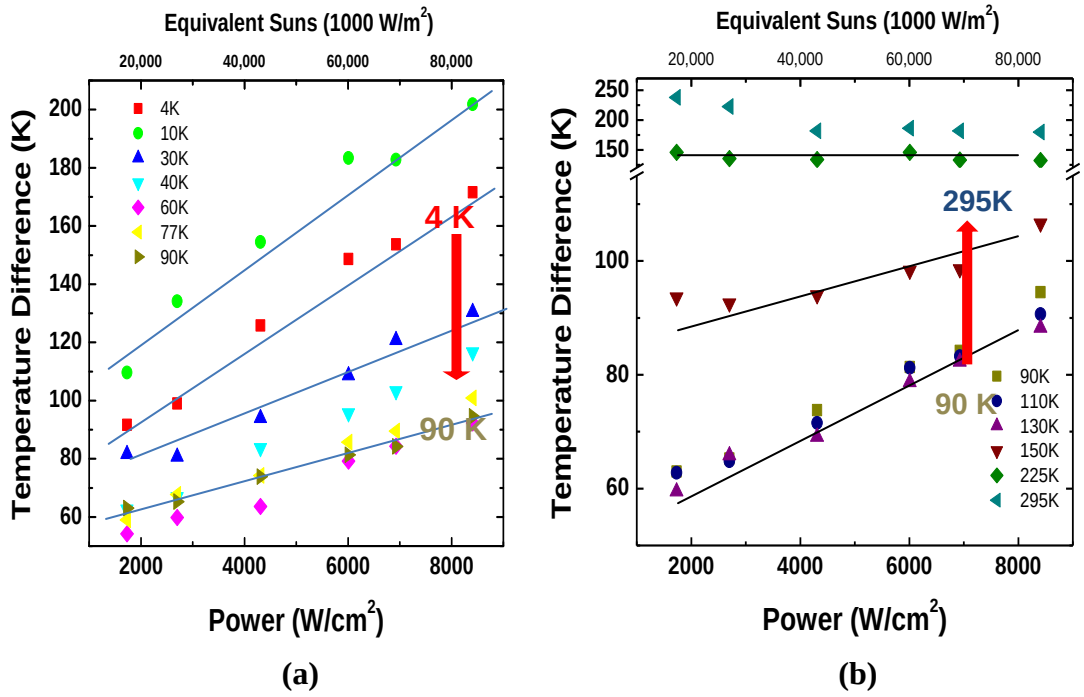

Figure 5.16: ΔT for different excitation power at different temperatures. Panels (a) and (b) show data for temperatures 4K to 90K and 90K to 295K, respectively.

5.10.3 Solar-cell structures

In addition to showing intended optical and structural properties, it is important that actual devices that comprise a SL for carrier generation show electrical characteristics of a solar cell. Also, CM effects can be ultimately observed via I-V characteristics of the solar-cell structures. One constraint at this stage of the research is the unavailability of an n-type dopant for AlAsSb and GaAsSb layers. N-type doping in Al/Ga antimonides is different than that of Al/Ga arsenides and needs a group VI element like S, Se or Te for doping[67]. In addition, compositional and interfacial inhomogeneities can lead to poor performance characteristics of the final device, therefore a reliable

systematic growth scheme must be investigated for high volume SLs. In a simple p-n junction solar cell, the photo generated carriers are free to move away from the junction. However, in the discussed SL structures, although hole confinement is low, photo generated and MEG electrons are confined within the large-gap AlAsSb barriers. Therefore it is necessary to explore a method for the fast extraction of the confined carriers.

Summary:

Doping efficiency in uniformly doped InGaAs epilayers was investigated for CMOS inverter application. Si and Be atoms were used as the n-type and p-type dopant, respectively. The goal was to understand doping limitations and achieve high concentrations ranging from $3\times10^{19}cm^{-3}$ to $5\times10^{19}cm^{-3}$. Carrier concentrations, determined through Hall measurements, show that low concentrations follow an Arrhenius relation. As the doping cell temperature increases, concentrations were found to drop below the Arrhenius projection for both n and p type doping, at typically used InGaAs growth conditions. The doping efficiency was improved by encouraging incorporation at substitutional sites by lowering the growth temperature, and allowing more dopant redistribution time by lowering the growth rate. At very high doping concentrations, the electron concentration appears to be limited by amphoteric behavior of Si and the hole concentration by surface segregation of Be. The maximum electron concentration achieved with Si doping is $4.8\times10^{19}cm^{-3}$ at a substrate temperature 365°C and a growth rate 0.63ML/s. The maximum hole concentration achieved with Be doping is $1.3\times10^{20}cm^{-3}$ at a substrate temperature 365°C and a growth rate 0.45 ML/s.

High density and high mobility strain-balanced $In_yGa_{1-y}As/In_xAl_{1-x}As$ QWs were grown for potential transistor application and ballistic electron studies. The key features of the QW are a deep and narrow well for one sub-band occupation and remote doping, to enhance mobilities at high well densities. A simple one sub-band theoretical model was used to calculate the required well population. The QW structures were grown by varying the supplied dopant density in conjunction with the spacer thickness to achieve

a high density and mobility of carriers in the well. The best structure has a room temperature (low temperature) mobility of 12,800cm^2/Vs (83,200cm^2/Vs) and density of $2.18\times10^{12}cm^{-2}$ ($2.16\times10^{12}cm^{-2}$). The density predicted by the theoretical approximation agrees well for structures with spacer thicknesses less than 10nm. The mobility of electrons was found to be enhanced by screening effects at high well densities. At lower densities, the mobility is determined by the relative strength of screening and ionized impurity scattering.

In superlattices, the effective bandgap of a QW can be tuned by confinement and miniband formation. An InAs/AlAsSb SL structure was designed to study hot carrier and CM effects, with a bandgap tuned to E_g ~0.8 eV and a barrier tall enough for the subband energy spacing to be larger than the bandgap. Initial structures were grown on GaAs (001) 2° off and InAs (001) substrates to determine the structural and optical properties of the SLs. The modeled structure with 2nm/2.4nm well/barrier thicknesses shows an effective bandgap of ~0.7eV for the SLs. Optical characterization of these structures show good agreement with the modeled values with a PL peak observed at ~0.8eV. Preliminary level structural analysis shows SL features close to the simulated peaks and a SL unit thickness of 2.7nm. A method to obtain specific AlAsSb alloy composition was also described. A GaAsSb absorber layer with an expected 0.7ev bandgap was grown and characterized. However, no significant intensity from GaAsSb layer was observed. The hot carrier population in the SLs was probed through photoluminescence and was found that carriers stay hot at temperatures higher than 90K. This could be due to negligible valence band offset compared to the thermal

energy of holes such that only a few holes are available for recombination. The next steps of this project are optimizing structures to maximize hot carrier population and growing solar-cell structures to study carrier multiplication.

Appendix

Appendix A

Summary of Initial Optical Structures:

Sample #	**Substrate**	**QW /barrier thickness(nm)**	**PL Signal**
t613	InAs	2.8/2	No
t652	GaAs	2.8/2	No
t650	InAs	2.8/2	No
t653	InAs	2.8/2	No
t665	GaAs	2.7/2	Yes

Additional Structures:

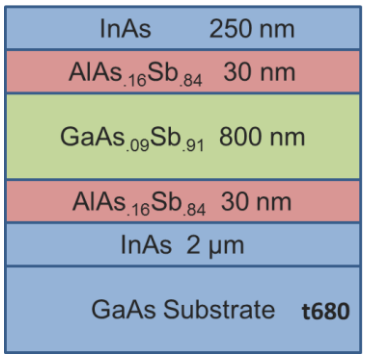

References:

1 *Molecular Beam Epitaxy: Fundamentals, Historical Background and Future Prospects*, Chapter 1, Secondo Franchi and Mohamed Henini, Elsevier-Oxford, (2013).

2 *Molecular Beam Epitaxy- Fundamentals and Current Status*, M. A. Herman and H. Sitter, Springer, (1996).

3 W. K. Liu and M. B. Santos, "Surface reconstructions of InSb(001) during molecular beam epitaxy," *Surface Science* **319**, 1–2, 172-183 (1994).

4 M.J. Yang, A.S. Bracker, B.R. Bennett, J.C. Culbertson, W.J. Moore, "Surface reconstruction phase diagrams for InAs, AlSb, and GaSb," *Journal of Crystal Growth* **220**, 384-392 (2000).

5 John R. Arthur, "Molecular beam epitaxy," *Surface Science* **500,** 1–3, 189-217 (2002).

6 S. J. Ingrey A. J. SpringThorpe, B. Emmerstorfer, P. Mandeville and W. T. Moore, "Measurement of GaAs surface oxide desorption temperatures," *Applied Physics Letters* **50**, 2 (1987).

7 *Quantum Dot Heterostructures*, M. Grundmann, D. Bimberg and N. N. Ledentsov, John Wiley and Sons, New York, (1999).

8 *Electronic and Optoelectronic Properties of Semiconductor Structures*, J. Singh, Cambridge University Press, (2003).

9 *Fundamentals of Semiconductors*, P. Y. Yu and M. Cardona, Springer, (2001).

10 *Theory of Optical Processes in Semiconductors: Bulk and Microstructures*, P. K. Basu, Clarendon press-Oxford, (1997).

11 *Wave Mechanics Applied to Semiconductor Heterostructures*, G. Bastard, France, (1988).

12 *Low Dimensional Semiconductors*, M. J. Kelly, Oxford University Press, (1995).

13 *Scanning Electron Microscopy, X-Ray Microanalysis and Analytical Electron Microscopy: A Laboratory Workbook*, C. E. Lyman et al., Plenum Press, New York, (1990).

14 *Scanning Electron Microscopy and X-ray Microanalysis*, Joseph Goldstein et al., Springer, (2003).

15 *High Resolution X-ray Diffractometry and Topography*, D. Keith Bowen and Brian K. Tanner, (1998).

16 *PC-MRD User's Guide for use with version 1.0 of the Philips PC-MRD software*, (1993).

17 *XRD data analysis of InSb/AlInSb heterostructures*, Prof. Bob Hauenstein from OSU.

18 *Characterization of Semiconductor Heterostructures and Nanostructures*, Carlo Lamberti, (2008).

19 "HallEffect: http://en.wikipedia.org/wiki/File:Hall_Effect_Measurement_Setup_for_Holes.png".

20 *Solid State Physics*, N. W. Ashcroft and D. N. Mermin, (1976).

21 L. J. Van der Pauw, "A method of measuring specific resistivity and Hall Effect of discs of arbitrary shape," *Philips Res. Repts*, **13**, 1 (1958).

22 *UV-VIS and Photoluminescence Spectroscopy for Nanomaterials Characterization*, Challa S. S. R. Kumar, Springer, (2013).

23 Suman Datta, Robert Chau, Amlan Majumdar, *Technical Digest, IEEE Compound Semiconductor Integrated Circuit Symposium,* Palm Springs, CA, 17-20, (Nov, 2005).

24 Han Zhao Feng Zhu, I. Ok, H. S. Kim, J. Yum, Jack C. Lee, Niti Goel, W. Tsai, C. K. Gaspe, and M. B. Santos, "High mobility HfO_2-based $In_{0.53}Ga_{0.47}As$ n-channel metal-oxide-semiconductor field effect transistors using a germanium interfacial passivation layer," *Appl. Phys. Lett* **93,** 132902 (2008).

25 Prashant Majhi Niti Goel, H. Wen, Michael Santos, Serge Oktyabrsky, Vadim Tokranov, Rama Kambhampati, Richard Moore, Feng Zhu, Jack Lee, Wilman Tsai, "$In_{0.53}Ga_{0.47}As$ based MOS capacitors with ALD ZrO_2 gate oxide demonstrating low gate leakage current and equivalent oxide thickness less than 1 nm," *Applied Physics Letters* **92**, 222904 (2008).

26 P. Majhi N. Goel, W. Tsai , M. Warusawithana , D.G. Schlom, M.B. Santos, J. Harris, Y. Nishi, "High-indium-content InGaAs metal-oxide-semiconductor capacitor with amorphous $LaAlO_3$ gate dielectric," *Applied Physics Letters*, **91**, 093509 (2007).

27 *Doping in III-V Semiconductors*, E. F. Schubert, Cambridge University Press, (1993).

28 *Diffusion of Berilliyum into Gallium Phosphide,* W.C. Ilegems M & O'Mara, (1972).

29 M. Ilegems, "Beryllium doping and diffusion in molecular-beam epitaxy of GaAs and $Al_x Ga_{1-x} As$," *J. Appl. Phys.*, **48**, 1278 (1977).

30 E. F. Schubert et al., "Be delta-doping of GaAs grown by MBE," *Journal of Applied Physics,* **67**, 1969 (1990).

31 T. Fujii et al., "Heavily Si-doped InGaAs lattice matched to InP grown by MBE," *Electronic Letters,* **22**, 4 (1986).

32 M. Beck, Y. Fedoryshyn, P. Kaspar, and H. Jaeckel, "Characterization of Si volume- and delta-doped InGaAs grown by molecular beam epitaxy," *Journal of Applied Physics* **107**, 093710 (2010).

33 M. B. Panish R. A. Hamm, R. N. Nottenburg, Y. K. Chen, and D. A. Humphrey "Ultrahigh Be doping of $In_{0.53}Ga_{0.47}As$ by low temperature molecular beam epitaxy," *Appl. Phys. Lett.*, **54**, 25 (1989).

34 S. Godey, S. Dhellemmes, A. Wilk, M. Zaknoune, and F. Mollot, "CBr_4 and Be heavily doped InGaAs grown in a production MBE system," *Journal of Crystal Growth* **278**, 1–4, 600-603 (2005).

35 S. L. Ren, J. J. Heremans, C. K. Gaspe, S. Vijeyaragunathan, T. D. Mishima, and M. B. Santos, "Aharonov–Bohm oscillations, quantum decoherence and amplitude modulation in mesoscopic InGaAs/InAlAs rings," *Journal of Physics: Condensed Matter* **25**, 43, 435301 (2013).

36 W. K. Liu, K. J. Goldammer, G. A. Khodaparast, S. C. Lindstrom, M. B. Johnson, R. E. Doezema, and M. B. Santos, "Electrical properties of InSb quantum wells remotely doped with Si," *J. Vac. Sci. Technol. B,* **16**, 3 (1998).

37 I. Vurgaftman and J. R. Meyer, "Band parameters for III–V compound semiconductors and their alloys," **89** ,11 (2001).

38 Mark S. Hybertsen, "Band offset transitivity at the InGaAs/InAlAs/InP(001) heterointerfaces," *Appl. Phys. Lett* , **58**, 1759 (1991).

39 T J Thornton, "Mesoscopic devices," *Reports on Progress in Physics* **58**, 3 (1995).

40 Y. Aharonov and D. Bohin, "Significance of Electromagnetic Potentials in the Quantum Theory," *The Physical Review* **115**, 3 (1959).

41 Hans J. Queisser, "Detailed balance limit for solar cell efficiency," *Materials Science and Engineering: B,* **159–160**, 0, 322-328 (2009).

42 *NREL Best research cell efficiencies*, (2013).

43 Matthew C. Beard, Kelly P. Knutsen, Pingrong Yu, Joseph M. Luther, Qing Song, Wyatt K. Metzger, Randy J. Ellingson, and Arthur J. Nozik, "Multiple Exciton Generation in Colloidal Silicon Nanocrystals," *Nano Letters*, **7**, 8, 2506-2512 (2007).

44 A De Vos, "Detailed balance limit of the efficiency of tandem solar cells," *J. Phys. D: Appl. Phys.*,**13**, 83 (1980).

45 *Semiconductor Device Fundamentals*, R. F Pierret, New York Addison-Wesley Publishing Company, Inc, (1996).

46 R. D. Schaller and V. I. Klimov, "High Efficiency Carrier Multiplication in PbSe Nanocrystals: Implications for Solar Energy Conversion," *Physical Review Letters* **92,** 18, 186601 (2004).

47 Randy J. Ellingson, Matthew C. Beard, Justin C. Johnson, Pingrong Yu, Olga I. Micic, Arthur J. Nozik, Andrew Shabaev, and Alexander L. Efros, "Highly Efficient Multiple Exciton Generation in Colloidal PbSe and PbS Quantum Dots," *Nano Letters* **5**, 5, 865-871 (2005).

48 James E. Murphy, Matthew C. Beard, Andrew G. Norman, S. Phillip Ahrenkiel, Justin C. Johnson, Pingrong Yu, Olga I. Mićić, Randy J. Ellingson, and Arthur J. Nozik, "PbTe Colloidal Nanocrystals: Synthesis, Characterization, and Multiple Exciton Generation," *Journal of the American Chemical Society* **128**, 10, 3241-3247 (2006).

49 R. Ulbricht, J. J. H. Pijpers, K. J. Tielrooij, A. Osherov, Y. Golan, C. Delerue, G. Allan and and M. Bonn, "Assessment of carrier-multiplication efficiency in bulk PbSe and PbS," *Nature Physics* **5**, 811 (2009).

50 Stuart K. Stubbs, Samantha J. O. Hardman, Darren M. Graham, Ben F. Spencer, Wendy R. Flavell, Paul Glarvey, Ombretta Masala, Nigel L. Pickett, and David J. Binks, "Efficient carrier multiplication in InP nanoparticles," *Physical Review B* **81,** 8, 081303 (2010).

51 D. König, K. Casalenuovo, Y. Takeda, G. Conibeer, J. F. Guillemoles, R. Patterson, L. M. Huang, and M. A. Green, "Hot carrier solar cells: Principles, materials and design," *Physica E: Low-dimensional Systems and Nanostructures* **42**, 10, 2862-2866 (2010).

52 R. Ross and A. Nozik, " Efficiency of hot-carrier solar energy converters," *J. Appl. Phys.* **53**, 3813 (1982).

53 S. Yagi and Y. Okada, "Fabrication of resonant tunneling structures for selective energy contact of hot carrier solar cell based on III-V semiconductors," *35th IEEE Photovoltaic Specialists Conference (PVSC)*, (2010).

54 G. Conibeer, N. J. Ekins-Daukes, J. F. Guillemoless, D. König, E. Cho, C. Jiang, S. Shrestha, and M. A. Green, " Progress on hot carrier cells," *Sol. Energy Mater. Sol. Cells* **93**, 713 (2008).

55 J. Tang, V. R. Whiteside, H. Esmaielpour, S. Vijeyaragunathan, T. D. Mishima, M. B. Santos, and I. R. Sellers, "Effects of localization of hot carriers in InAs/AlAsSb quantum wells," *Applied Physics Letters* (in press).

56 Alexey Semenov, Olga G. Lyublinskaya, Victor A. Solov'ev, Boris Ya Meltser, and Sergey V. Ivanov, "Surface segregation of Sb atoms during molecular-beam epitaxy of InSb quantum dots in an InAs(Sb) matrix," *Journal of Crystal Growth* **301–302**, 0, 58-61 (2007).

57 Ramesh Babu Laghumavarapu, Paul J. Simmonds, Meng Sun, Andrew Lin, Charles J. Reyner, Baolai Liana, and Diana L. Huffaker, "Structural and optical properties of InAs/AlAsSb quantum dots with GaAs(Sb) cladding layers," *Appl. Phys. Lett.* **100**, 243108, (2012).

58 P. Cristea, Y. Fedoryshyn, and H. Jäckel, "Growth of AlAsSb/InGaAs MBE-layers for all-optical switches," *Journal of Crystal Growth* **278**, 1–4, 544-547 (2005).

59 R. Gargallo-Caballero M. Ulloa, M. Bozkurt, M. del Moral, A. Guzma´n, and and A. Hierro P.M. Koenraad, *Phys. Rev. B* **81** ,165305, (2010).

60 J. Steinshnider, J. Harper, M. Weimer, C. H. Lin, S. S. Pei, and D. H. Chow, "Origin of Antimony Segregation in Strained-Layer Superlattices," *Physical Review Letters* **85**, 21, 4562-4565 (2000).

61 F. Gentya A. Wilka, B. Fraisseb, G. Boissiera, P. Grecha, M. El Gazoulia,P. Christolc, J. Oswaldd, T. Simecekd, E. Huliciusd, A. Joullie´, "MBE growth of InAs/InAsSb/AlAsSb structures for mid-infrared lasers," *Journal of Crystal Growth* **223**, 341-348 (2001).

62 G. Almuneau, E. Hall, S. Mathis, and L. A. Coldren, "Accurate control of Sb composition in AlGaAsSb alloys on InP substrates by molecular beam epitaxy," *Journal of Crystal Growth* **208** ,1–4, 113-116 (2000).

63 Hao Ye, Lu Li, Robert T. Hinkey, Rui Q. Yang, Tetsuya D. Mishima, Joel C. Keay, Michael B. Santos, and Matthew B.Johnson, "MBE growth optimization of InAs (001) homoepitaxy," *Journal of Vacuum Science & Technology B: Microelectronics and Nanometer Structures* **31**, 3 (2013).

64 T. Zederbauer, G. Strasser, Institute of Solid State Electronics, Vienna University of Technology, Austria, (2014).

65 Yang-Seok Yoo et al., "Simple analysis method for determining internal quantum efficiency and relative recombination ratios in light emitting diodes," *Applied Physics Letters* **102**, 211107 (2013).

66 A. Le Bris, L. Lombez, S. Laribi, G. Boissier, P. Christol, and J. F. Guillemoles, "Thermalisation rate study of GaSb-based heterostructures by continuous wave photoluminescence and their potential as hot carrier solar cell absorbers," *Energy & Environmental Science* **5**, 3, 6225-6232 (2012).

67 G. Tuttle S. Subbanna, H. Kroemer, "N- type doping of gallium antimonide and aluminum antimonide grown by molecular beam epitaxy using lead telluride as a tellurium dopant source," *Journal of Electronic Materials* **17,** 4, 297-303 (1988).